Structural and Oxidation State Changes of the Photosystem II Manganese Complex in Four Transitions of the Water Oxidation Cycle ($S_0 \rightarrow S_1$, $S_1 \rightarrow S_2$, $S_2 \rightarrow S_3$, and $S_{3,4} \rightarrow S_0$) Characterized by X-ray Absorption Spectroscopy at 20 K and Room Temperature[†]

M. Haumann,*[,‡] C. Müller,[‡] P. Liebisch,[‡] L. Iuzzolino,[§] J. Dittmer,[§] M. Grabolle,[‡] T. Neisius,[||] W. Meyer-Klaucke,[⊥] and H. Dau*[,‡]

FB Physik, Freie Universität Berlin, Arnimallee 14, D-14195 Berlin, Germany, Philipps-Universität Marburg, Karl-von-Frisch-Strasse, D-35032 Marburg, Germany, ESRF, BP 220, 38043 Grenoble Cedex, France, and EMBL Outstation Hamburg, Notkestrasse 85, D-22603 Hamburg, Germany

Received June 23, 2004; Revised Manuscript Received October 8, 2004

ABSTRACT: Structural and electronic changes (oxidation states) of the Mn_4Ca complex of photosystem II (PSII) in the water oxidation cycle are of prime interest. For all four transitions between semistable S-states ($S_0 \rightarrow S_1$, $S_1 \rightarrow S_2$, $S_2 \rightarrow S_3$, and $S_{3,4} \rightarrow S_0$), oxidation state and structural changes of the Mn complex were investigated by X-ray absorption spectroscopy (XAS) not only at 20 K but also at room temperature (RT) where water oxidation is functional. Three distinct experimental approaches were used: (1) illumination-freeze approach (XAS at 20 K), (2) flash-and-rapid-scan approach (RT), and (3) a novel time scan/sampling-XAS method (RT) facilitating particularly direct monitoring of the spectral changes in the S-state cycle. The rate of X-ray photoreduction was quantitatively assessed, and it was thus verified that the Mn ions remained in their initial oxidation state throughout the data collection period (>90%, at 20 K and at RT, for all S-states). Analysis of the complete XANES and EXAFS data sets (20 K and RT data, S_0-S_3, XANES and EXAFS) obtained by the three approaches leads to the following conclusions. (i) In all S-states, the gross structural and electronic features of the Mn complex are similar at 20 K and room temperature. There are no indications for significant temperature-dependent variations in structure, protonation state, or charge localization. (ii) Mn-centered oxidation likely occurs on each of the three S-state transitions, leading to the S_3 state. (iii) Significant structural changes are coupled to the $S_0 \rightarrow S_1$ and the $S_2 \rightarrow S_3$ transitions which are identified as changes in the Mn−Mn bridging mode. We propose that in the $S_2 \rightarrow S_3$ transition a third Mn−(μ-O)$_2$−Mn unit is formed, whereas the $S_0 \rightarrow S_1$ transition involves deprotonation of a μ-hydroxo bridge. In light of these results, the mechanism of accumulation of four oxidation equivalents by the Mn complex and possible implications for formation of the O−O bond are considered.

Photosynthetic water oxidation, the light-driven oxidation of two water molecules yielding reducing equivalents, protons, and the byproduct dioxygen, takes place in photosystem II (PSII),[1] a cofactor−protein complex embedded in the thylakoid membrane of higher plants, green algae, and cyanobacteria. The specific locus of water oxidation is a tetramanganese complex bound to amino acid residues at the lumenal side of the D1 protein subunit of PSII; it presumably contains one calcium and, perhaps, one chloride ion as further cofactors (*1*, *2*). The Mn_4Ca complex, including the ligating amino acid residues, is commonly denoted as the oxygen-evolving complex (OEC). In several decades of intense research, a wealth of relevant insights has been obtained by extensive characterization of the reaction kinetics (*2*). However, at the atomic level, the intricate mechanism of the water oxidation reaction is only insufficiently understood.

Driven by the sequential absorption of four light quanta by PSII, the OEC cycles through five increasingly oxidized states, denoted as S_0-S_4 (*3*). Each $S_i \rightarrow S_{i+1}$ transition

[†] Financial support from the Deutsche Forschungsgemeinschaft (SFB 498, Projects C6 and C8) and from the Bundesministerium für Bildung und Wissenschaft (Grant 05KS1KEA/6) is gratefully acknowledged.

* To whom correspondence should be addressed. H.D.: FB Physik, Freie Universität Berlin, Arnimallee 14, D-14195 Berlin, Germany; telephone, +49 (0)30 8385 3581; fax, +49 (0)39 8385 6299; e-mail, holger.dau@physik.fu-berlin.de. M.H.: FB Physik, Freie Universität Berlin, Arnimallee 14, D-14195 Berlin, Germany; telephone, +49 (0)-30 8385 6101; fax, +49 (0)39 8385 6299; e-mail, haumann@physik.fu-berlin.de.

[‡] Freie Universität Berlin.

[§] Philipps-Universität Marburg.

[||] ESRF.

[⊥] EMBL Outstation Hamburg.

[1] Abbreviations: ADRY, acceleration of the deactivation reactions of the water-splitting enzyme system Y; Chl, chlorophyll; EPR, electron paramagnetic resonance spectroscopy; EXAFS, extended X-ray absorption fine structure; FCCP, carbonyl cyanide *p*-trifluoromethoxyphenylhydrazone; FT, Fourier transform; fwhm, full width at half-maximum; MES, 2-(*N*-morpholino)ethanesulfonic acid; OEC, oxygen-evolving complex; PPBQ, phenyl-*p*-benzoquinone; PSII, photosystem II; Q_A, primary quinone acceptor of PSII; RT, room temperature; S_i, intermediate states of the water oxidation cycle; XAS, X-ray absorption spectroscopy; XANES, X-ray absorption near-edge structure; Y_Z, tyrosine 161 of the D1 subunit of PSII.

10.1021/bi048697e CCC: $30.25
Published on Web 01/22/2005

comprises the abstraction of one electron from the OEC by an oxidized tyrosine residue, Y_Z^{ox} [D1-Tyr-161 (*4*)]. The Y_Z^{ox} radical is created by the transfer of an electron from Y_Z to the oxidized primary donor, P_{680}^+, a chlorophyll cation radical previously created in the primary light reaction by electron transfer. The S_1 state of the OEC is stable in the dark, and the higher S-states, with the exception of the S_4 state, are stable for up to several minutes at room temperature (*5*). S_4 decays spontaneously (without additional light input) to form S_0 with liberation of a dioxygen molecule.

X-ray absorption spectroscopy (XAS) can provide information about the nuclear geometry and some electronic properties (e.g., oxidation states) of biological metal centers (*6*−*10*). Empirically, the position of the K-edge on the energy scale has been found to be correlated with the formal oxidation state of Mn (*7*, *11*−*14*). The shape of the edge reflects the coordination number (number of ligands in the first coordination sphere) and coordination geometry (for a review, see ref *7*). The oscillatory structure observed in the EXAFS region of an XAS spectrum can be attributed to a free-electron backscattering phenomenon (*15*). The final state wave function of the photoelectron created by X-ray absorption is discussed in terms of an outgoing wave centered at the absorber position and backscattering of this free-electron wave by neighboring atoms of the first few coordination spheres. These neighboring atoms are thus denoted as "backscatterers". EXAFS analysis allows for the determination of absorber−backscatterer distances at an accuracy that may be better than 0.02 Å. First-sphere ligands are always detected in the EXAFS; more distant atoms may be resolvable, and atoms more than 5 Å from the absorber cannot usually be detected. The EXAFS oscillations originating from heavy backscatterers (Mn and Ca) are different from the EXAFS oscillation of light backscatterers (O, N, and C) and significantly stronger so that heavy backscatterers at distances of <4 Å are usually visible (*6*−*10*, *15*). The XAS method is particularly well-suited to monitoring of structural and oxidation state changes at the metal sites of metalloenzymes which occur in the course of the catalytic cycle (*16*, *17*).

Biological metal centers mainly have been studied by XAS at cryogenic temperatures, precluding direct observation of structural changes by time-resolved XAS measurements. Furthermore, at low temperatures, redox equilibria might be shifted, leading to a modified location of some radical states; a temperature dependence of functionally relevant spin states and protonation equilibria can hardly be excluded (*18*, *19*). A promising approach to solving these problems is the investigation of the catalytic cycle of metalloenzymes by XAS on noncrystalline samples at temperatures at which biological catalysis actually takes place, i.e., at or close to room temperature (*16*, *20*−*22*). The oxidation state and structural changes of the Mn complex have been investigated by XAS mostly at temperatures below 100 K (see refs *7*, *13*, *14*, *16*, and *23*−*28*). At cryogenic temperatures, electron transfer between Mn and Y_Z is impaired and water oxidation is inactive (*29*, *30*); specific low-temperature effects on the structure and/or redox properties of PSII cofactors have been reported (*29*−*35*). A more pronounced decrease in the rate of electron transfer from Mn to Y_Z^{ox} during the oxygen-evolving transition, $S_{3,4} \rightarrow S_0$, below temperatures close to 0 °C has been attributed to changes at the Mn complex (*36*, *37*); thermal barriers in the interconversion between substates of the OEC could lead to temperature-dependent properties (*38*−*40*). Thus, one can imagine that during illumination of PSII at low temperatures or during freezing of previously illuminated PSII samples, states of the Mn complex are formed which differ from the reactive states at room temperature. To judge the relevance of low-temperature data for the mechanism of water oxidation, it clearly is important to compare the structural and electronic properties of the Mn complex at cryogenic temperatures with those at room temperature (RT).

The structural and electronic properties of the Mn complex and the changes occurring in the course of the S-cycle are still debated. Diverging low-temperature XAS results on S_3 have been obtained (*23*, *25*, *41*−*44*). The S_0 state investigated by low-temperature EXAFS in ref *45* was populated by a protocol involving ADRY reagents and thus may not necessarily be identical to the "native" S_0 state created solely by illumination. First, structural RT data on S_3 have been presented (RT EXAFS spectra in ref *21*), but neither the S_0 structure nor the oxidation state changes (RT XANES spectra) were addressed. In this investigation, we study the structure and oxidation state of the Mn complex for all four S-states by XAS at cryogenic temperatures (20 K) and at room temperature. Whereas EXAFS represents the primary structural tool used in these investigations, the XANES comprises significant information about the electronic structure (see above). Since the changes in electronic and geometric structure in the S-cycle are intimately interrelated, we combine the XANES and EXAFS analysis of all four S-states in a single work. The thus obtained results facilitate a comprehensive discussion of the structural and oxidation state changes in the S-cycle and the emerging mechanistic implications.

MATERIALS AND METHODS

Sample Preparation and S-State Population. PSII-enriched membrane particles (*46*) were prepared from market spinach using glycine betaine as a stabilizer in all media (*41*, *47*). The oxygen evolution activity of the preparations under saturating white-light illumination was 1200−1400 μmol of O_2 (mg of Chl)$^{-1}$ h^{-1} at 28 °C. For the preparation of PSII membrane multilayers, PSII membrane particles were dissolved at 1 mg/mL Chl in a medium containing 15 mM NaCl, 5 mM $MgCl_2$, 5 mM $CaCl_2$, 1 M betaine, 10% v/v glycerol, and 25 mM MES (pH 6.2). Glycerol was added to maximize the amount of centers which produce the "multiline" EPR signal (*48*, *49*) which can be attributed to S_2 under illumination at the expense of the EPR $g = 4$ signal which has been attributed to a modified S_2 state (*50*, *51*). The $g = 4$ signal was not detectable in our PSII samples (data not shown). An artificial electron acceptor, PPBQ, was added at a final concentration of 200 μM. Multilayer samples of PSII membranes on Kapton foil (sample dimensions ca. 15 mm × 2.5 mm) were prepared by a centrifugation procedure (*41*) or by a drop-and-dry protocol (unpublished).

The centrifugation procedure of ref *41* yielded samples which were employed in the XAS measurements at 20 K and in the flash-and-rapid-scan XAS experiments at room temperature. Immediately after the preparation, these multilayers (thickness of ∼75 μm) were simultaneously il-

luminated from both sides by a single actinic flash from two xenon flash lamps (fwhm ∼ 5 μs, λ > 400 nm). In combination with the subsequent dark adaptation period, this protocol maximizes the proportion of centers in S_1 and the amount of centers with oxidized Y_D (*41*, *47*). After the preflash, samples were partially dehydrated by drying over silica gel in a desiccator at a reduced air pressure (400 mbar) for 2 h at 4 °C and in complete darkness (dark adaptation period of 2 h). For preparation of samples enriched in higher S-states, three different procedures were used. (1) The samples later used for XAS experiments at 20 K were illuminated from both sides simultaneously by zero, one, two, or three xenon flashes (λ > 400 nm) to yield samples enriched in the S_1, S_2, S_3, or S_0 state, respectively. Only for S_2 EXAFS samples were dark-adapted multilayer samples illuminated by actinic white light (400 nm < λ < 750 nm) at 200 K in a dry ice/ethanol bath for 2 min to yield PSII in S_2. After illumination, samples were rapidly frozen (within <1 s) in liquid nitrogen (for a maximum of 14 days) until they were used at the synchrotron radiation source (illumination-freeze or flash-freeze approach of the S-state population). (2) In the flash-and-rapid-scan XAS experiments, the higher S-states were populated by applying laser flashes (see below and refs *16*, *20*, and *21*) to the samples at room temperature immediately before the start of data collection (flash spacing of 400 ms, last flash given ∼200 ms before the opening of the fast beam shutter and the start of the XAS scans). For sampling-XAS experiments, multilayer samples were produced directly before the XAS measurements at the beamline from stock solutions of PSII membrane particles (6−8 mg of Chl/mL) by the drop-and-dry procedure. (3) Enrichment of the higher S-states was achieved by simultaneous laser flash illumination (frequency-doubled Q-switched Nd:YAG laser; Quantel Brilliant, fwhm of 5 ns, 532 nm, ∼150 mJ per pulse) of the sample from both sides. During flash illumination, the sample was kept at room temperature and exposed to the X-ray beam as previously described (*16*, *20*, *21*, *41*). By oxygen polarimetry on redissolved multilayer samples, it was verified that the oxygen evolving capacity of PSII was almost unchanged (±10%) after both procedures of multilayer preparation and partial dehydration of samples. Each XAS sample contained ∼100−150 μg of chlorophyll and an estimated Mn concentration of ∼1 mM.

X-ray Absorption Measurements. (1) XAS measurements at the Mn K-edge at 20 K were performed at the EMBL bending-magnet EXAFS beamline D2 at HASYLAB (DESY, Hamburg, Germany) during six measuring periods using an energy-resolving solid state 13-element germanium detector (Canberra) for fluorescence detection as described elsewhere (*41*). The Si111 crystal monochromator was detuned to 70% of the maximal flux. Samples were kept in a helium cryostat (Oxford) at 20 K under ∼200 mbar of helium gas. The X-ray spot size on the samples was ∼5 mm × 1 mm. The scan duration (6400−7100 eV) was ∼20 min.

XAS measurements at room temperature were carried out at undulator beamline ID26 of the European Synchrotron Radiation Facility (ESRF) in Grenoble, France, during three measuring periods. Manganese X-ray absorption spectra were measured by monitoring the excited X-ray fluorescence perpendicular to the incident beam by a PIN photodiode (3.8 cm^2 active area, Eurisys Meassures). A 10 μm chromium filter and a 10 μm aluminum foil in front of the photodiode largely suppressed scattered X-rays and visible light, respectively. Samples were exposed to plain air at the temperature (18 ± 2 °C) of the climatized experimental hutch of the beamline.

(2) Flash-and-rapid-scan XAS spectra at room temperature were collected by simultaneous scanning of a Si220 crystal monochromator (detuned to 70% of the maximal flux, scan range of 6500−7100 eV, X-ray spot size on the sample of ∼1 mm × 1 mm) and the undulator gap [rapid-scan mode of ID26 (*52*)] as previously described (*20*, *22*). Only one scan with a duration of 12 s was performed per sample spot on dark-adapted samples (∼12 separate spots per sample); on laser-flash-illuminated samples, only a single scan was performed. A total of 25 different batches of multilayer samples from nine different PSII membrane particle preparations was used. The X-ray flux was reduced by a factor of 25−35 with respect to the maximal flux by thin aluminum and Kapton foil filters. When filters were used, it was checked by XAS scans on sample holders covered with several layers of Kapton that no signals due to Mn contamination of the filter (or of any other origin) were detectable (absence of any Mn K-edge feature).

(3) Sampling-XAS measurements (*20*) rely on the monitoring of the time course of the X-ray fluorescence intensity (20 ms acquisition time per data point) at a fixed excitation energy (time scan of fluorescence). Time scans were carried out at 100 excitation energies ranging between 6539 and 6930 eV. Between 5 and 10 time scans were carried out at each excitation energy employing a fresh sample for each scan (total of ∼750 samples). During the time scans, a series of nanosecond laser flashes (flash spacing of 400 ms; see above) was fired. Samples were positioned in the X-ray beam by a computer-controlled sample changer. A rapid beam shutter blocked the X-ray beam during automated sample exchange and positioning. At both synchrotron radiation sources, the excitation angle between the electric field vector of the X-ray beam and the normal to the surface of the PSII multilayers was 55° [magic angle (*53*)]. Energy calibration was facilitated by simultaneous measurements of the absorption of the narrow pre-edge feature (centered at 6543.3 eV) of a $KMnO_4$ powder sample mounted in front of a detector at the end of the beamline.

Data Evaluation for the 20 K and Flash-and-Rapid-Scan Techniques. The energy axis of each raw XAS spectrum was calibrated using Gaussian simulations of the pre-edge peak of $KMnO_4$ to determine precisely its energy position; the accuracy of the energy calibration procedure itself is estimated to be better than ±0.1 eV (*22*, *41*). Then, XAS spectra were averaged after appropriate weighting to account for the different signal-to-noise ratios resulting from slight variations in sample thickness, scattering background, and X-ray beam intensity. The final XAS spectra represent the average of 30−80 individual scans. XAS spectra were normalized and EXAFS oscillations extracted as outlined in refs *7* and *54*. The energy scale of the EXAFS oscillations was transformed to a wavevector scale (k scale) using an energy threshold (E_0) of 6540 eV. EXAFS data were averaged to yield 100 data points per spectrum equally spaced on a k scale and then weighted by k^3 to compensate for the drop in EXAFS oscillations with energy.

Data Evaluation for the Sampling-XAS Technique. For the collection of sampling-XAS spectra at room temperature, the

protocol outlined in detail in ref *20* was employed. (i) Rapid XAS scans (6500−7100 eV) with a duration of 12 s were performed on dark-adapted samples with the Mn complex in S_1 (no flash illumination) at room temperature. In these measurements, the X-ray flux was reduced by filters so that the lag phase observed in the time course of X-ray photoreduction of the Mn complex in S_1 lasted for ~20 s (*21*). From these rapid scan spectra, a room-temperature reference spectrum of S_1 was derived by normalization as outlined above. (ii) Time scans of fluorescence with a duration of 5 s (20 ms per data point) were performed on dark-adapted samples; during the first seconds of the time scans, three laser flashes spaced by 400 ms were fired. (iii) After the time scan, on the same sample spot a rapid XAS scan (6500−7100 eV) with a duration of 12 s was performed under the same conditions. The raw fluorescence−time scan traces were normalized, and the data points falling into a time interval of 400 ms before flash 1 and after flashes 1−3 were averaged. Sampling-XAS spectra were constructed from the averaged data points using the continuous-scan S_1 spectrum as a reference (basically, the normalized fluorescence changes induced by flashes 1−3 were added to the S_1 reference spectrum to yield the XAS spectra after these flashes). The room-temperature sampling-XAS spectra were thus obtained relative to the S_1 reference spectrum by data collection within a time interval of only 400 ms after the laser flash that initiated the respective S-state transition.

Simulation of EXAFS Spectra. Spectra were simulated by a least-squares procedure using the in-house software SimX (*55*). Complex phase functions for different elements in the various shells of backscatterers were calculated using FEFF [version 7 (*56*)] on the basis of a model which comprises two di-μ-oxo-bridged Mn pairs interconnected by a mono-μ-oxo bridge. The amplitude reduction factor, S_0^2, was 0.85; in the simulations, a value for E_0 of 6547 eV was consistently used. The quality of the least-squares fits was judged by calculation of the Fourier-filtered *R*-factor (R_F) after the curve fit itself, as described elsewhere (*22*). Exclusively, the unfiltered k^3-weighted EXAFS oscillations were used in the fit process. Fourier-isolated EXAFS oscillations (as obtained by back-transformation of a limited distance range of Fourier transforms into the *k* space) were not employed in the simulation process because interference phenomena may contribute to the EXAFS of the Mn complex due to the presence of oscillations with closely spaced distances, thereby causing misleading simulation results (*7*, *57*).

RESULTS

The Mn complex of PSII may become significantly reduced upon X-ray irradiation (photoreduction), even during XAS measurements carried out at 20 K employing moderate irradiation intensities (*58*). In XAS measurements at room temperature, Mn photoreduction is accelerated (*16*, *20*−*22*). The initial photoreduction of the Mn complex at 20 K and at room temperature was characterized for all S-states (see the Supporting Information). According to the results of this quantitative characterization, experimental conditions have been optimized so that only negligible X-ray-induced modifications of the PSII Mn complex took place within the duration of the XAS experiments. The fraction of the Mn ions that remained in their initial oxidation exceeded 90% in all experiments discussed below (see the Supporting Information, I).

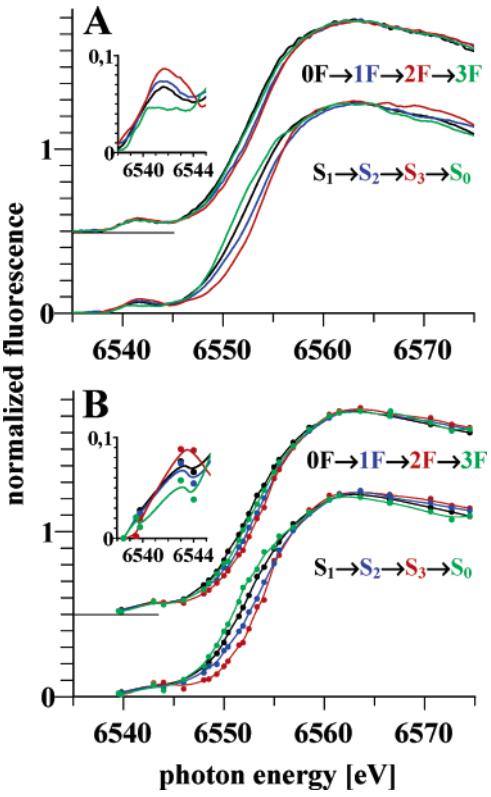

FIGURE 1: XANES spectra of the Mn complex in four S-states. (A) K-Edge spectra measured at 20 K for samples prepared by the flash-freeze approach. Top traces are spectra without flash illumination (0F, black) and with illumination by one (1F, blue), two (2F, red), and three (3F, green) flashes of light. Bottom traces are deconvoluted K-edge spectra of the four S-states. (B) K-Edge spectra obtained by the sampling-XAS approach at RT. Top traces are spectra obtained for data collected within 400 ms on a dark-adapted sample and after illumination by zero to three flashes. Colors are as in panel A. Bottom traces are deconvoluted K-edge spectra of the four S-states. Dots represent measured data points, and lines are spline curves through the data points drawn to guide the eye. The insets in panels A and B show the magnified pre-edge region of the deconvoluted spectra.

XANES Spectra of the Mn Complex in Its Four S-States. XANES spectra of the Mn complex were recorded using two methods. (1) The flash-freeze approach was employed for S-state population; XANES spectra were recorded at 20 K. (2) At RT, time scans of the X-ray fluorescence were recorded during illumination with a sequence of laser flashes, for a set of selected X-ray energies. Figure 1 (top traces in each panel) shows the XANES spectra after zero, one, two, and three flashes measured at 20 K (Figure 1A) and RT (Figure 1B). For a quantitative discussion of the shifts in the K-edge position and of changes in the shape of the K-edge spectra upon each S-state transition, deconvolution of the flash spectra is necessary to yield the pure S-state spectra (see the Supporting Information, II).

The deconvoluted XANES spectra (bottom traces in each panel of Figure 1) measured at 20 K (Figure 1A) and RT (Figure 1B) are remarkably similar. Inspection of the difference spectra (Figure 2) confirms that the same spectral changes are observed for XAS data collection on frozen samples at 20 K and for immediate data collection at RT (and within 400 ms of the flash-induced transition). We note

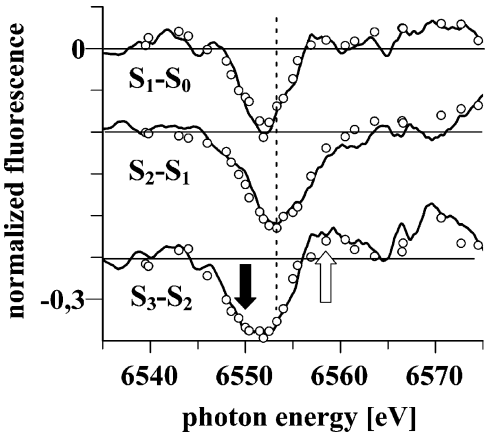

FIGURE 2: XANES differences spectra. (—) Differences in the edge spectra of Figure 1A for the pure S-states, collected at 20 K. (○) Differences in the edge spectra of Figure 1B for the pure S-states, obtained by the time scan−sampling-XAS approach at RT. The dotted line has been drawn approximately through the center of the negative peak in the $S_2 - S_1$ difference spectrum, to emphasize the shifts in the energy of the maximal changes in the XANES spectra.

Table 1: Changes in the K-Edge Energies of the Mn Complex upon Four S-State Transitions[a]

	K-edge energy of the S_1 state[b] (eV ± 0.1)	difference in K-edge energies of the S-states[b] (eV)			
data set	E_1	$E_1 - E_0$	$E_2 - E_1$	$E_3 - E_2$	$E_0 - E_3$
20 K	6551.62	0.58	0.76	0.71	−2.05
RT	6551.79	0.57	0.79	0.70	−2.06

[a] The values correspond to spectra measured at 20 K and RT by the sampling-XAS technique. [b] K-Edge energies were derived by the "integral method" (*7*) from deconvoluted spectra that can be attributed to the pure S-states (see Figure 1) using integration limits of 0.15−1.0 of spectra previously normalized to an edge jump of unity.

that the XANES and difference spectra of Figures 1 and 2 are remarkably similar to the data of ref *43*. Visual inspection of Figure 1 reveals that the upshift in the X-ray edge is similar in magnitude for each of the three oxidizing transitions ($S_0 \rightarrow S_1$, $S_1 \rightarrow S_2$, and $S_2 \rightarrow S_3$). The Mn K-edge energy of each S-state was quantified by the "integral method" described elsewhere (*7*, *59*) (Table 1).

In contrast to the $S_1 \rightarrow S_2$ transition, during the $S_2 \rightarrow S_3$ transition a particularly pronounced shift is observed in the rising part of the edge (particularly negative value in the difference spectra at 6550 eV, Figure 2). Furthermore, only during the $S_2 \rightarrow S_3$ transition is a signifcant increase in the absorption around 6558 eV detected (positive value in the difference spectra). We note that, in the 20 K data, the crossover point of the S_2 and S_3 spectra and the extent of absorption increase at 6558 eV depend critically on the accuracy of the normalization of the XANES spectra. In this respect, the RT sampling-XAS method is superior because *changes* in the absorption become directly detectable in the time scan data (discussed below) and the difference spectra are clearly less susceptible to normalization inaccuracies. The good agreement between 20 K and RT data thus also confirms the achieved accuracy in the normalization of the 20 K data.

In summary, by the analysis of Mn K-edge spectra of the four S-states measured at 20 K and, for the first time, at room temperature, we consistently find a significant shift of the K-edge position to a higher energy, on all three oxidizing transitions (Table 1). The magnitude of each of these shifts (~0.7 eV) is compatible with oxidation of one Mn ion in each of the three oxidizing transitions. The specific changes in the shape of the X-ray edge observed during the $S_2 \rightarrow S_3$ transition are straightforwardly explained by assuming a transition from five-coordinated Mn^{III} to six-coordinated Mn^{IV} (see the Discussion).

Direct Observation of Spectral Changes by the Time Scan−Sampling-XAS Approach. It represents a specific advantage of the time scan−sampling-XAS approach that by recording time scans of the excited X-ray fluorescence during application of a laser flash sequence even small flash-induced changes become directly observable (Figure 3). At the selected X-ray energy, the direction and relative extent (relative to the other flash-induced transitions) of the changes in the X-ray absorption associated with the individual flash-induced transition can be immediately judged, prior to subsequent data analysis which eventually leads to the normalized spectra shown in Figure 1B.

Figure 3 (top) shows, for selected excitation energies, time scans of the X-ray fluorescence during which three laser flashes were fired. In the rising part of the X-ray edge (Figure 3, 6549 eV), the first flash ($S_1 \rightarrow S_2$) and the second flash ($S_2 \rightarrow S_3$) induce absorption decreases essentially identical in magnitude, whereas at 6553 eV the second flash decrease is significantly smaller. At 6560 eV, immediately prior to the principal edge maximum, the first flash induces an absorption increase, whereas the second flash causes a decrease proving a crossover of the S_2 and S_3 spectrum between 6553 and 6560 eV. Thus, the main characteristics of the XANES changes associated with $S_1 \rightarrow S_2$ and $S_2 \rightarrow S_3$ transitions are directly visible in the time scan data.

In Figure 3, the fluorescence time scans in the EXAFS range of 6635−6860 eV indicate only minor absorption changes upon the first flash ($S_1 \rightarrow S_2$), but relatively pronounced absorption changes upon the second ($S_2 \rightarrow S_3$) and third flash ($S_{3,4} \rightarrow S_0$), immediately suggesting that, in comparison to the $S_1 \rightarrow S_2$ transition, the $S_2 \rightarrow S_3$ and $S_{3,4} \rightarrow S_0$ transitions are associated with significant structural changes. By EXAFS simulations of complete spectra, we find that the EXAFS amplitude at 6820 eV is closely related to the magnitude of the second peak of Fourier-transformed spectra. In the time scan of Figure 3, at 6820 eV a relatively high absorption after two flashes (S_3) and a particularly low absorption after three flashes (S_0 populated) are clearly visible. This direct observation reinforces the crucial finding, discussed below, that the amplitude of the second FT peak is approximately the same in S_1 and S_2, particularly high in S_3, and particularly low in S_0.

EXAFS Spectra: Not Deconvoluted. In Figure 4, low-temperature EXAFS spectra of dark-adapted samples and of samples exposed to one to three illuminations (illumination-freeze approach, Figure 4A) as well as room-temperature spectra obtained by two different methods [flash-and-rapid-scan approach (Figure 4B) and sampling-XAS approach (Figure 4C)] are shown. Visual comparison of Figure 4 reveals the following points of special importance.

(i) 20 K versus RT Spectra. In the room-temperature spectra, FT peaks I and II are broadened and their magnitudes are reduced with respect to those of the 20 K spectra (Figure

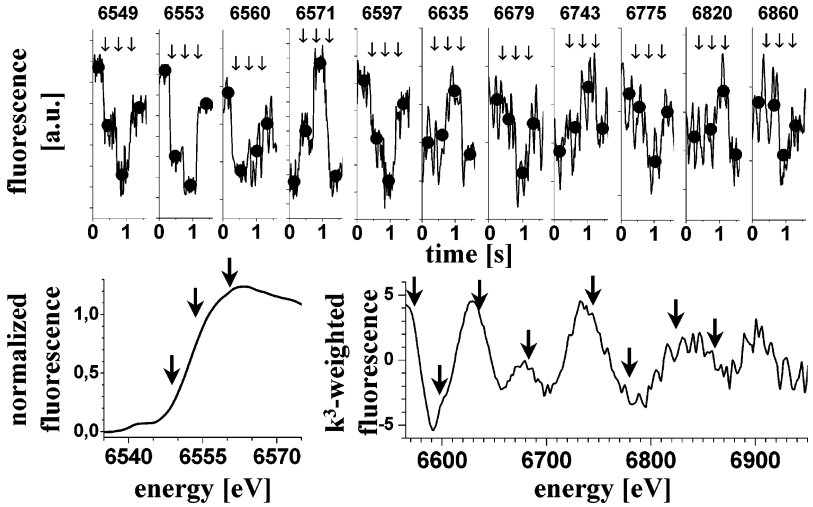

FIGURE 3: Laser flash-induced X-ray fluorescence changes during the S-state cycle. The top panel shows time scans of X-ray fluorescence at selected excitation energies in the region of the K-edge and in the EXAFS. The time resolution was 20 ms per point. Arrows denote the points in time where the three laser flashes were fired. Dots represent the fluorescence levels obtained by averaging of the data points before, between, and after the flashes. The shown transients have been obtained by averaging of transients measured at excitation energies within ranges of 2 eV (K-edge region) and 10−15 eV (EXAFS region) around the indicated center energies. The bottom left panel shows the room-temperature K-edge spectrum from dark-adapted samples. The bottom right panel shows the respective k^3-weighted EXAFS oscillations on an energy scale. Arrows indicate the respective excitation energies of the traces shown in the top part of the figure.

4A). Otherwise, the changes (amplitude of EXAFS oscillations at higher *k* values, magnitude of FT peaks I and II) associated with the individual S-state transition are qualitatively similar in the 20 K and RT data.

(ii) Changes in the Second Fourier Peak. The magnitude of the EXAFS oscillations for *k* values greater than 7 Å^{-1} is approximately equal in S_1 and S_2, increased in the two-flash sample, and lowered again by application of the third flash. The same holds for the magnitude of FT peak II, in all three sets of spectra.

Structural Information Acquired by EXAFS Simulations. The spectra shown in Figure 4 were simulated by an unbiased approach, employing only two shells of backscatterers (O/N and Mn). This two-shell approach already roughly accounts for the main EXAFS features, namely, for the two most prominent FT peaks. Consistently, we find that in the dark-adapted Mn complex and after one and three illuminations the number of Mn−Mn vectors ∼2.7 Å in length per Mn atom in the complex is relatively close to one (Table 2). After two light flashes, however, when S_3 is predominantly populated, a number of these vectors close to 1.5 is determined.

The raw EXAFS oscillations (Figure 4, left) were deconvoluted (see the Supporting Information, II−IV) to yield the spectra that can be attributed to the pure S-states (Figure 5). (We refrain from analyzing the deconvoluted sampling-EXAFS spectra because of their limited *k* range.) By using the simple two-shell approach (Table 3A), we find that the overall Mn−O/N distance in the primary ligand shell of Mn (direct ligands) decreases when advancing from S_0 over S_1 to S_2, and remains approximately the same in S_3. The EXAFS coordination number of the primary O/N ligation shell determined by curve fitting is slightly increased in S_3, providing a (weak) indication of an increase in the number of Mn ligands.

The two-shell simulations of the 20 K spectra yield a coordination number of the Mn−Mn interactions ∼2.7 Å in length relatively close to 1 in the S_1, S_2, and S_0 states (Table 3A, 20 K). In contrast to this result, in S_3 the obtained value is slightly greater than 1.5. One 2.7 Å interaction per Mn atom suggests the presence of two Mn pairs separated by 2.7 Å, whereas a value of 1.5 points toward the presence of three such pairs in the Mn_4 complex. The mean Mn−Mn distance is approximately the same (2.71 Å) in S_1 and S_2, slightly larger in S_3 (2.74 Å), and clearly larger (2.76−2.77 Å) in S_0. The Debye−Waller parameter of the Mn−Mn interaction in S_0 is approximately twice as large as in the other S-states, pointing toward the presence of two Mn−Mn vectors of significantly different length, but with a mean value close to 2.76 Å.

Simulation of the EXAFS spectra collected at RT using the two-shell approach described above results in basically the same coordination numbers and distances for the Mn−Mn shell and a similar trend for the first-coordination sphere parameters. As anticipated, the absolute values of the Debye−Waller parameter, σ, are increased due to thermally activated dynamic disorder. Also at RT, in comparison to those of the other S-states, the Debye−Waller parameter is found to be significantly increased in S_0. In conclusion, the 20 K and RT EXAFS data point toward the same structural changes in the course of the S-state cycle.

Table 3B refers to an advanced, knowledge-based simulation approach described in the following and more extensively discussed elsewhere (*7*, *22*, *57*).

First Coordination Sphere (primary ligands to Mn). The XANES spectra of the PSII−Mn complex point toward the presence of mostly six-coordinated and perhaps some five-coordinated Mn ions (*7*). Because of the likely presence of several short Mn−μ-O distances (1.7−1.9 Å) and a broad range of longer terminus−ligand distances (1.9−2.4 Å) in the mixed-valence complex, a particularly broad distribution of Mn−ligand distances is anticipated. In Table 3A, the radial distribution function of the first-sphere ligands is modeled by a single Gaussian function, where the width of this function is given by σ, the Debye−Waller parameter. This representation of the radial distribution is not fully adequate;

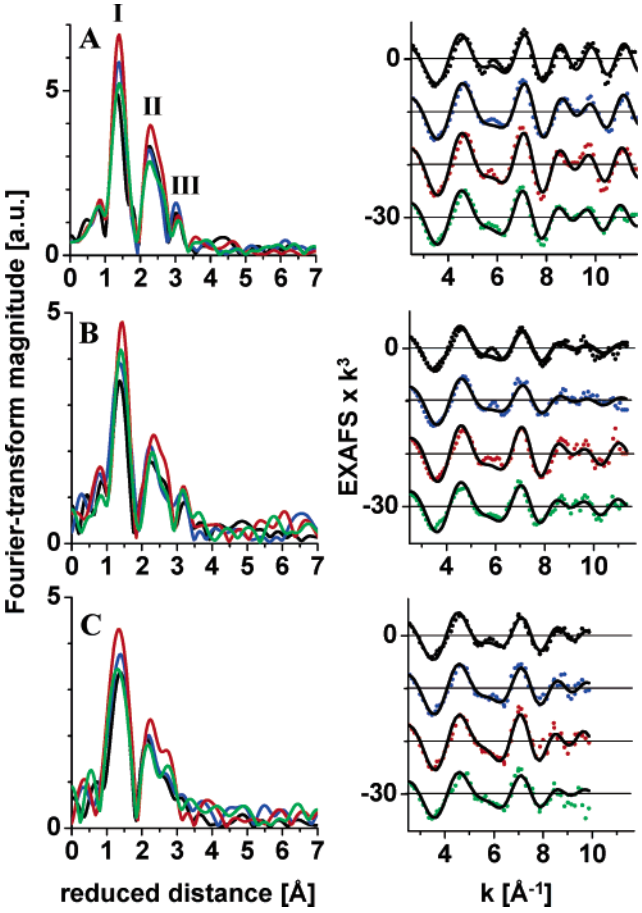

FIGURE 4: EXAFS spectra of the Mn complex after illumination of PSII samples. (A) Spectra measured at 20 K on samples prepared by the illumination-freeze approach. (B) Spectra measured at room temperature using the flash-and-rapid-scan technique. (C) Spectra measured at room temperature by the sampling-XAS technique. Experimental data are depicted with dots; smooth lines represent simulations with parameters given in Table 2. The right column shows k^3-weighted EXAFS oscillations in the k space after zero (black), one (blue), two (red), or three (green) illuminations (see Materials and Methods for details). The left column shows the respective Fourier transforms (FTs) of the experimental EXAFS oscillations. FTs were calculated with cosine windows extending over 10% of the k space at low or high k values and for k values ranging from 1.8 to 11.8 Å^{-1} (A), from 1.8 to 11.4 Å^{-1} (B), and from 1.8 to 9.9 Å^{-1} (C).

it leads to a systematic underestimation of the coordination number and mean Mn−ligand distance, and to low-quality simulations (relatively high R_F value) (*7*, *22*). Therefore, in Table 3B, the radial distribution of first-sphere ligands is described by a sum of two Gaussian functions formally corresponding to a simulation with two distinct subshells of first-sphere ligands. To minimize the number of variable simulation parameters, the individual coordination numbers of the subshells were fixed (meaning invariable) in the course of the simulations. Their sum was chosen to be between 5 and 6, namely, 5.5, to account for the possibility that some of the Mn ions are six-coordinated whereas others may be five-coordinated. For S_1−S_3, good fits were obtained for equal values of the two subshell coordination numbers, whereas for S_0, only a pronouncedly asymmetric distribution leads to high-quality simulations (see Table 3C). We note that by using different approaches to model the distance distribution function of the first coordination sphere by two

Table 2: Results of Two-Shell Simulations of EXAFS Spectra Collected after Zero, One, Two, or Three Illuminations[a]

		N_i (per Mn)/R_i(Å)/σ_i(Å)		
		Mn−O,N[b]	Mn−Mn[b]	R_F (%)
20 K	0F	4.55/1.858/0.112	1.24/2.712/0.045	27.2
	1F[c]	4.48/1.849/0.091	0.96/2.711/0.033	21.7
	2F	4.79/1.848/0.087	1.41/2.736/0.047	20.4
	3F	4.65/1.857/0.099	1.25/2.742/0.065	22.3
RT (rapid-scan XAS)	0F	4.17/1.849/0.114	1.09/2.716/0.082	35.2
	1F	4.23/1.842/0.116	1.02/2.708/0.084	36.8
	2F	4.68/1.844/0.098	1.49/2.730/0.079	33.6
	3F	4.37/1.850/0.104	1.20/2.741/0.080	28.5
RT (sampling-XAS)	0F	4.07/1.851/0.111	1.13/2.713/0.069	23.7
	1F	4.27/1.842/0.108	1.09/2.712/0.066	24.3
	2F	4.89/1.839/0.104	1.32/2.738/0.062	20.9
	3F	4.29/1.845/0.112	1.24/2.742/0.090	32.8

[a] N_i, coordination number per Mn atom; R_i, distance between the absorbing Mn and the backscatterer; σ_i, Debye−Waller parameter; R_F, filtered error factor (*22*) (calculated for a range of reduced distances of 1−3.5 Å). Fits of k^3-weighted EXAFS oscillations were performed for k values ranging from 1.8 to 11.8 Å^{-1} (20 K), from 1.8 to 11.4 Å (RT, rapid-scan EXAFS), and from 1.8 to 9.9 Å (RT, sampling-EXAFS). E_0 = 6547 eV. The shown parameters have been derived from simulations of the spectra depicted in Figure 4. [b] N_i (per Mn)/R_i (Å)/σ_i (Å). [c] Continuously illuminated at 200 K as described in Materials and Methods.

subshells of backscatters, the fit results for the more distant coordination shells are only marginally affected.

Second Coordination Sphere (atoms linked to Mn via a single intervening atom). Recent crystallographic results (*60*, *61*) confirm previous findings of mutagenesis (*62*−*65*) and XAS experiments (*7*, *23*, *26*) that the Mn ligand environment in the Mn_4Ca complex of PSII is characterized by a high number of bridging ligands and a relatively low number of ligating amino acid residues (1−2 per Mn ion). Consequently, the number of light atoms (O, N, and C) in the second coordination sphere of the X-ray-absorbing Mn is low, so their contribution to the EXAFS oscillations in the distance range from 2.5 to 3.4 Å becomes negligibly small in the presence of strong EXAFS oscillations stemming from backscattering by Mn and Ca atoms. The second Fourier peak is dominated by the particularly strong 2.7 Å Mn−Mn EXAFS (*7*, *23*, *26*) already considered in the simulation approach of Table 3A. In the refined simulation approach, an additional contribution from backscattering by heavy atoms around 3.3 Å is considered which affects both the second and third FT peaks. The presence of a Ca ion 3.3−3.5 Å from, presumably, two Mn ions has been demonstrated (*66*−*69*). Additionally, a Mn−Mn distance of >3 Å is also assumed to be present (*7*, *57*). By a joint fit of a time series of spectra (*57*) or by analysis of the linear dichroism in the EXAFS of partially oriented samples (*23*, *54*), it became practicable to resolve the individual Mn−Ca and Mn−Mn distances. By simulation of a single EXAFS spectrum, however, this remains impossible. Therefore, in the refined simulation approach, these two shells are merged into a single backscatterer shell. We note that, because of the significant distance heterogeneity, this backscatterer shell contributes only weakly to the EXAFS oscillations (*7*). Therefore, an independent determination of coordination number and σ value cannot be achieved. We employed a fixed value of 1.0 for the EXAFS coordination number which corresponds to a single Mn−Mn vector and two Mn−Ca vectors per tetramanganese complex.

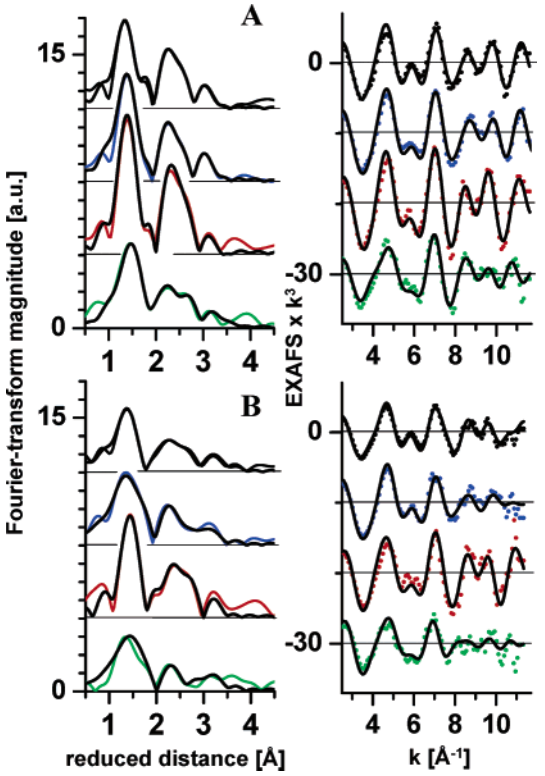

FIGURE 5: EXAFS spectra of the Mn complex in four S-states. (A) Spectra measured at 20 K (illumination-freeze approach). (B) Spectra measured at room temperature by the flash-and-rapid-scan technique. The depicted spectra result from deconvolution of the spectra shown in Figure 4; they can be attributed to the pure S-states. In the left column, the FTs of the experimentally obtained EXAFS data are displayed using colored solid lines; in the right column, the experimental EXAFS oscillations are depicted using colored dots (black for S_1, blue for S_2, red for S_3, and green for S_0). Black lines represent simulations of the experimental spectra using the parameters listed in Table 3B (see the text for details). The respective Fourier transforms were calculated with parameters given in the legend of Figure 4.

Third Coordination Sphere (more remote scatterers). Peak III in the Fourier-transformed EXAFS spectra also seemingly contains contributions from the Mn−Mn,Ca vectors >3 Å in length and, most likely, also from backscatterers at ~3.6 Å. The inclusion of a shell of light backscatterers at ~3.6 Å improves the fit quality significantly (*7*, *22*, *57*). In the EXAFS of Mn-depleted PSII containing only two Mn ions at a Mn−Mn distance of 2.7 Å, the magnitude of the third Fourier peak is found to be only slightly diminished, strongly suggesting that light backscatterers make a major contribution to the third FT peak (*57*, *70*). We tentatively assign this distance to the first-sphere oxygen (but third-sphere ligand with respect to the X-ray-absorbing Mn) bound to Mn in the second coordination sphere of the X-ray-absorbing Mn according to the $Mn^{absorber}$−μ-O−$Mn^{secondsphere}$−$O^{scatterer}$ model. Again, a fully independent determination of the EXAFS coordination number and σ value is not possible; high-quality fits are obtained for EXAFS coordination numbers of 2−4.

The refined, knowledge-based approach results in significantly improved simulations (Table 3B). With respect to the 2.7 Å Mn−Mn vector, however, the conclusions remain unaffected. Both 20 K and RT results indicate the presence of two such vectors per Mn_4 complex in S_1, S_2, and S_0 (EXAFS coordination number of ~1.0), but three in S_3 (EXAFS coordination number of ~1.5). In S_0, the mean Mn−Mn distance is significantly elongated and the σ value significantly increased, pointing to the presence of one Mn−Mn distance close to 2.7 Å and of a second one greater than 2.8 Å.

Number of 2.7 Å Mn−Mn Distances per Mn_4 Complex. To corroborate the determined values for the EXAFS coordination numbers of the 2.7 Å Mn−Mn vector, the extent of correlation between the coordination number and Debye−Waller parameter was systematically studied (Figure 6). By varying these parameters of the 2.7 Å shell, we investigated whether the best fits shown in Table 3B correspond to the absolute minima in the fit error. Figure 6 shows the error factors (R_F) obtained from the respective simulations of the 20 K data using a five-shell approach (see the figure legend) for all four S-states. The frequently used Fourier isolation method was avoided because it is potentially misleading (*7*). Instead, a particularly stringent way of exploring the error surface was used: The coordination number and σ^2 value of the 2.7 Å shell were varied in small steps, and for each ($N_{2.7}$ and $\sigma_{2.7}{}^2$) pair, a full simulation (meaning curve fit) was carried out using the refined simulation approach described above. The alternative way to explore the error surface by variation of $N_{2.7}$ and $\sigma_{2.7}{}^2$ without a renewed curve fit is clearly less meaningful because the fixed simulation parameters of neighboring shells introduce a distinct bias.

Noteworthily, the error shown in Figure 6 is the Fourier-filtered *R*-factor which represents the deviation between experimental spectra and simulations in percent for the contributions in the EXAFS corresponding to the FT distance range of 1.0−3.5 Å. (This R_F value was calculated by means of a Fourier isolation approach, but only after completion of the fit process; the fit process itself did not involve any Fourier filtering.) By calculation of the R_F value for the FT distance range from 2 to 3.0 Å, the deepness of the absolute minima increases pronouncedly so that in S_1, for example, the lowest R_F values for $N_{2.7}$ and $N_{2.7}$ of 1.0 and 1.5 become 6 and 14, respectively, corresponding to in increase in R_F of ~130% (*71*), as compared to an increase of ~35% in Figure 6.

The contour plots of the error factor shown in Figure 6 are similar for S_1 and S_2 but differ distinctly for S_3 and S_0 spectra. In S_1 and S_2, minima of the error are found at $N_{2.7}$ values of ~0.75 and ~1.0, respectively, but only the latter value is associated with a positive $\sigma_{2.7}{}^2$ value. In S_3, minima are found at $N_{2.7}{}^2$ values of 1.5, 1.25, and 1.0, but only for the minimum at 1.5 is the $\sigma_{2.7}{}^2$ value positive. Since zero or negative σ^2 values can be dismissed as physically unreasonable, the contour plots indicate that the value of $N_{2.7}$ is 1.0 in S_1 and S_2 but increases from 1 to 1.5 from S_2 to S_3.

In S_0, the contour plot reveals an absolute minimum at 1.0 and two relative minima at $N_{2.7}$ values of ~0.7. In the Mn_4 complex of PSII, reasonable values for $N_{2.7}$ are multiples of 0.5 (0.5, 1.0, 1.5, ...) so that relative minima around 0.7 suggest a "real" $N_{2.7}$ value of either 0.5 or 1.0. At an $N_{2.7}$ value of 0.5, however, $\sigma_{2.7}{}^2$ is approximately zero (physically unreasonable) and the error is significantly increased. Therefore, and because the absolute error minimum equals 1.0, we tentatively conclude that an $N_{2.7}$ value of 1.0 represents the more likely alternative. We note that because of the shallowness of the error surface in S_0, an $N_{2.7}$ value of 0.5 cannot be excluded rigorously.

Table 3: Simulation Parameters for the EXAFS Spectra of the Pure S-States[a]

		N_i (per Mn)/R_i(Å)/σ_i(Å)					
		Mn−O,N[b]	Mn−O,N[b]	Mn−Mn[b]	Mn−Mn,Ca[b]	Mn−O,N,C[b]	R_F (%)
		(A) Two-Shell Simulation Approach					
20 K	S_1	4.49/1.851/0.110		1.16/2.712/0.041			26.5
	S_2	4.48/1.849/0.091		0.96/2.711/0.033			21.1
	S_3	4.82/1.844/0.082		1.59/2.742/0.043			23.9
	S_0	4.65/1.872/0.103		1.09/2.763/0.072			37.9
RT	S_1	4.13/1.850/0.113		1.08/2.715/0.087			36.6
	S_2	4.33/1.840/0.111		1.12/2.705/0.083			38.5
	S_3	4.80/1.849/0.078		1.62/2.735/0.061			38.4
	S_0	4.25/1.855/0.125		1.10/2.776/0.100			44.0
		(B) Five-Shell Simulation Approach					
20 K	S_1	2.75[c]/1.812/0.074	2.75[c]/1.978/0.098	0.96/2.716/0.028	1.00[c]/3.218/0.105	2.50[c]/3.663/0.076	12.9
	S_2	2.75[c]/1.813/0.081	2.75[c]/1.919/0.094	0.93/2.714/0.031	1.00[c]/3.256/0.093	2.50[c]/3.628/0.085	13.8
	S_3	2.75[c]/1.803/0.031	2.75[c]/1.938/0.058	1.49/2.744/0.039	1.00[c]/3.156/0.104	2.50[c]/3.711/0.087	12.7
	S_0	4.50[c]/1.872/0.104	1.00[c]/2.297/0.039	0.90/2.774/0.064	1.00[c]/3.112/0.089	2.50[c]/3.653/0.073	17.2
RT	S_1	2.75[c]/1.833/0.091	2.75[c]/2.017/0.154	1.04/2.711/0.088	1.00[c]/3.135/0.105[c]	2.50[c]/3.693/0.082[c]	18.2
	S_2	2.75[c]/1.801/0.114	2.75[c]/1.909/0.108	0.93/2.702/0.078	1.00[c]/3.171/0.105[c]	2.50[c]/3.650/0.082[c]	21.1
	S_3	2.75[c]/1.797/0.155	2.75[c]/1.865/0.047	1.53/2.741/0.071	1.00[c]/3.076/0.105[c]	2.50[c]/3.674/0.082[c]	19.9
	S_0	4.50[c]/1.853/0.118	1.00[d]/2.375/0.055	1.02/2.762/0.102	1.00[c]/3.198/0.105[c]	2.50[c]/3.673/0.082[c]	24.5
		(C) Specific Simulation Approaches					
20 K	S_1	2.75[c]/1.809/0.073	2.75[c]/1.961/0.095	0.50[c]/2.686/0.025[c] 0.50[c]/2.739/0.025[c]	1.00[c]/3.207/0.114	2.50[c]/3.645/0.076	12.3
	S_2	2.75[c]/1.805/0.089	2.75[c]/1.901/0.091	0.50[c]/2.684/0.025[c] 0.50[c]/2.738/0.025[c]	1.00[c]/3.250/0.097	2.50[c]/3.613/0.080	14.3
	S_3	3.00[c]/1.804/0.045	3.00[c]/1.939/0.066	1.47/2.743/0.039	1.00[c]/3.166/0.099	2.50[c]/3.716/0.078	12.8
		3.00[c]/1.806/0.050	3.00[c]/1.938/0.068	1.51/2.743/0.038	0.50[c]/3.169/0.075	2.50[c]/3.697/0.091	12.7
		3.00[c]/1.805/0.048	3.00[c]/1.937/0.069	0.50[c]/2.727/0.025[c] 0.50[c]/2.727/0.025[c] 0.50[c]/2.774/0.025[c]	0.50[c]/3.182/0.063	2.50[c]/3.704/0.080	13.5
	S_0	4.50[c]/1.872/0.103	1.00[c]/2.296/0.039	0.50[c]/2.720/0.025[c] 0.50[c]/2.841/0.025[c]	1.00[c]/3.102/0.078	2.50[c]/3.645/0.074	15.2

[a] N_i, coordination number per Mn atom; R_i, distance between the absorbing Mn and the backscatterer; σ_i, Debye−Waller parameter; R_F, filtered error factor calculated for R values ranging between 1 and 3.5 Å (*22*). Shown are the results of simulations of the deconvoluted k^3-weighted EXAFS oscillations of four S-states (see Figure 5). Simulations were performed on spectra measured at 20 K and RT by the flash-and-rapid-scan technique. [b] N_i (per Mn)/R_i (Å)/σ_i (Å). [c] Not varied in the simulations. [d] Continuously illuminated at 200 K as described in Materials and Methods.

Estimate of Individual Mn−Mn Distances. Because the thermal activation of dynamic contributions becomes negligible small at 20 K, the σ values of the 20 K data set (Table 3) mostly reflect static distance heterogeneities determined by chemical factors. It is shown above that in S_1, S_2, and S_0 two Mn−Mn vectors contribute to the 2.7 Å EXAFS, whereas in S_3, there are three such vectors per Mn_4 complex. For these Mn−Mn vectors ~2.7 Å in length, the σ value mostly reflects the length differences between the individual contributing vectors. To illustrate this aspect, simulations were carried out in which each individual vector of the 2.7 Å shell is described by an individual length and a common, relatively small, intrinsic σ value is used for the individual shells (Table 3C). (This intrinsic σ value accounts for the static distance spread due to an assumed continuous distribution of multiple conformations of the Mn complex and its protein environment. We note that its precise value is unknown, and the choice of this intrinsic σ value affects the then determined distances.)

Using the approach described above, we determine individual Mn−Mn distances of 2.69 and 2.74 Å in S_1 and S_2, respectively, demonstrating that the length of the two contributing Mn−Mn vectors may differ by ~0.05 Å. Seemingly not only the average distance but also the individual distances remain approximately unchanged when the complex advances from S_1 to S_2. The simulation result obtained for S_3 illustrates that one of the three contributing Mn−Mn vectors could be as long as 2.77 Å, whereas the other two are 2.73 Å in length. In S_0, seemingly the length of one of the contributing vectors is close to 2.72 Å, whereas the length of the second one is greater than 2.80 Å. (The fit results in Table 3 indicate a distance of 2.84 Å. Because of significant noise contributions in the S_0 data, the accuracy of the fit results is poorer than in the other S-states. A distance shorter than 2.8 Å, however, cannot be reconciled with the EXAFS data.)

DISCUSSION

Temperature Dependence. For the first time, it became possible to measure XANES spectra at room temperature (for all S-states), facilitating judgment about the role of temperature-dependent redox equilibria. The XANES spectra collected at 20 K and room temperature are found to be identical within the noise limit, suggesting that in all S-states the localization of the accumulated oxidizing equivalents is temperature-independent. Furthermore, the same basic structural features with respect to the primary ligands of Mn (coordination number and geometry) are suggested by the XANES detected at 20 K and RT. The EXAFS spectra collected at 20 K and RT differ visibly, but only due to thermally activated nuclear motions at RT (see also ref *22*). The simulation results indicate that there are only insignificant temperature-dependent changes in the absorber−backscatterer distances. Thus, for all S-states, temperature-dependent changes in the protonation state of the di-μ-oxo bridges can be safely excluded. In conclusion, structure and

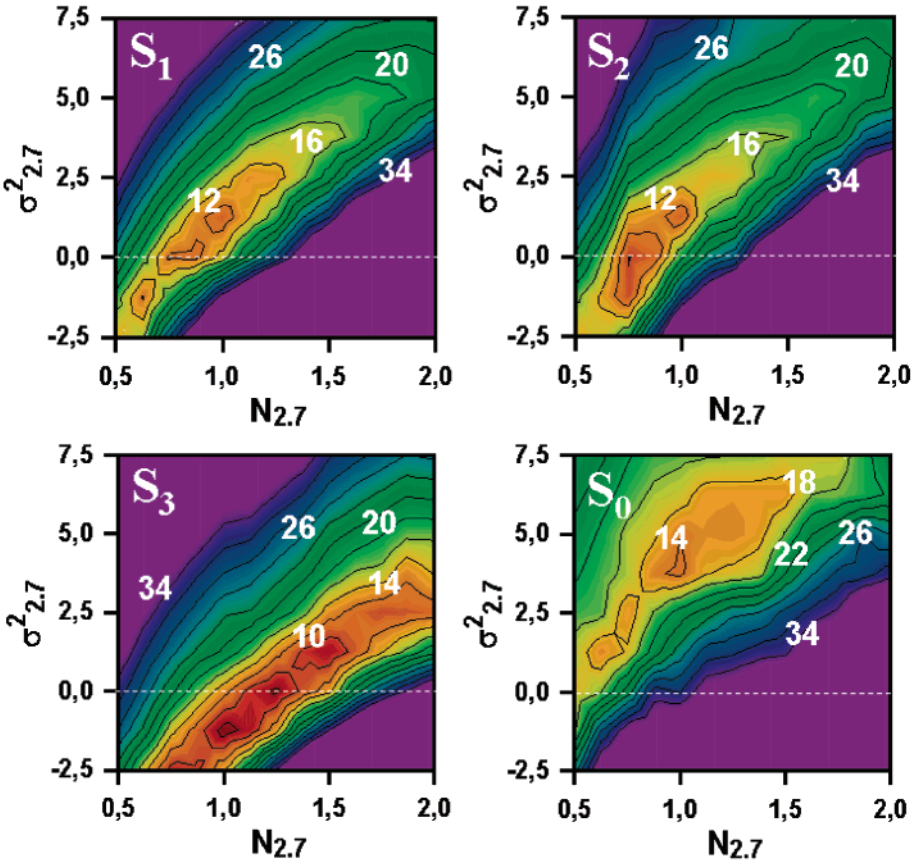

FIGURE 6: Contour plots of the R_F values from simulations of EXAFS spectra of the four S-states. The R_F values are depicted for the respective pairs of σ^2 (Debye−Waller parameter, in square angstroms) and $N_{2.7}$ (EXAFS coordination number of the 2.7 Å Mn−Mn vector, per absorbing Mn ion) values in the form of a contour plot. The spacing between the lines is 1.5%. Simulations have been performed using a five-shell approach (see Table 3B) for all S-state spectra measured at 20 K shown in Figure 5A (for details, see the text). Numbers in represent rounded values of R_F at the indicated positions. Red and orange colors denote the lowest R_F values and, thus, the best fits. Below the dashed lines, the Debye−Waller parameter acquires physically unreasonable negative values.

crucial electronic properties (oxidation states) of the PSII−Mn complex seem to be largely temperature independent. For all S-states, it holds that a temperature-dependent redox isomerism is not observed and that there are no indications for relevant protonation state differences.

XANES and Oxidation State Changes in the S-State Cycle. Single-electron oxidation of Mn causes a shift of the K-edge to higher energies which mostly falls in the range of 0.4−1.2 eV (normalized to allow for comparison with the Mn_4 complex of PSII) (*7*, *11*−*14*, *72*, *73*). In this work, we determine for three oxidizing transitions an upshift of the edge position by 0.6−0.8 eV for data collected at 20 K and RT (Table 1), pointing toward one-electron oxidation of Mn on the $S_0 \rightarrow S_1$, $S_1 \rightarrow S_2$, and $S_2 \rightarrow S_3$ transitions.

The occurrence of Mn-centered oxidation in the $S_2 \rightarrow S_3$ transition is still disputed (*24*, *25*, *39*, *41*, *44*). In a previous XAS study at 20 K (*41*), we determined for this transition an edge shift by 0.6−1.3 eV, depending on the details of the deconvolution procedure and the method used to determine edge positions. It has been argued (*43*) that the relatively large $S_2 \rightarrow S_3$ shift of our previous work (*41*) originates from imprecise deconvolution resulting from the neglect of centers blocked in S_2. In the work presented here, we estimated the fraction of PSII blocked in S_2 on the basis of Chl fluorescence measurements and considered this fraction explicitly in the deconvolution procedure (Supporting Information, II). The thus obtained edge shift value of 0.7 eV is at the lower limit of the range considered in ref *41* but remains suggestive of Mn-centered oxidation also in the $S_2 \rightarrow S_3$ transition.

Comparison of the difference spectra for the oxidizing transition of Figure 2 and of the ones reported in ref *43* reveals that principally the same changes in the XANES are observed in both investigations. However, using the inflection-point (IP) method (edge position energy defined as the zero-crossing point of the second derivative), in ref *43* edge shifts of 2.1 eV for the $S_0 \rightarrow S_1$ transition, 1.1 eV for the $S_1 \rightarrow S_2$ transition, and 0.3 eV for the $S_2 \rightarrow S_3$ transition have been reported. As demonstrated and extensively discussed elsewhere (*7*), the IP method may be generally inappropriate for mixed-valence complexes, and its use is particularly problematic whenever the shape of the K-edge spectra becomes modified as a consequence of changes in the coordination geometry. [Also, the innovative K_β fluorescence analysis in refs *43* and *81* appeared to support the absence of Mn-centered oxidation in the $S_2 \rightarrow S_3$ transition; however, (i) it is doubtful that the 3p−3d exchange interaction presumably underlying the oxidation state sensitivity of the K_β fluorescence (*82*) is insensitive to a coordination number change, and (ii) the data presented in ref *43* are significantly affected by X-ray photoreduction and the extrapolation to the zero-exposure limit is problematic.]

Undisputed specifics of the XANES changes in the $S_2 \rightarrow S_3$ transition are a particularly pronounced absorption

decrease at 6550 eV (marked by the filled arrow in Figure 2) and an absorption increase at 6558 eV (empty arrow in Figure 2). By full-multiple-scattering simulations (FMS) of edge spectra on the basis of self-consistent potentials (*75*) supplemented by comparative molecular orbital (MO) consideration, we recently have found that the changes in edge shape and position observed for the $S_2 \rightarrow S_3$ transition are straightforwardly explained by a transition from five-coordinated Mn^{III} to six-coordinated Mn^{IV} (*7*, *76*). Comparative experimental studies on synthetic $Mn^{III}L_5$ complexes versus the $Mn^{IV}L_6$ complex have not been approached, but studies on complexes of other transition metals (e.g., refs *77*−*80*) support the rationale outlined in refs *7* and *76*.

The transformation of $Mn^{III}L_5$ to $Mn^{IV}L_6$ is in agreement with the observation that, in contrast to the other oxidizing S-state transitions, the average Mn−ligand bond length becomes not shortened in the $S_2 \rightarrow S_3$ transition. Furthermore, the formation of an additional μ-oxo bridge during the $S_2 \rightarrow S_3$ transition provides a straightforward rationale for explaining the coordination number change as discussed further below.

We conclude that the XANES data do not provide any indication for a ligand radical in S_3. Further investigations may be required to answer definitively whether and to what extent spin density is acquired by Mn ligands during the $S_2 \rightarrow S_3$ transition.

The following absolute redox state assignments are supported by various spectroscopic studies of S_1 and S_2 and, to a lesser extent, S_0 (*7*, *13*, *23*, *27*, *41*, *43*, *44*, *83*, *84*; but see also refs *85* and *86*): $Mn_4^{II,III,IV,IV}$ or $Mn_4^{III,III,III,IV}$ for S_0, $Mn_4^{III,III,IV,IV}$ for S_1, $Mn_4^{III,IV,IV,IV}$ for S_2, and $Mn_4^{IV,IV,IV,IV}$ for S_3. The above conclusions about oxidation state *changes* and the following discussion of structural changes do not depend on the absolute Mn oxidation state assignment.

Consistency of the EXAFS Results. In this work, we assess structural changes of the Mn complex on the basis of EXAFS spectra that have been obtained by three different methods: (1) at RT using the time scan−sampling-XAS technique, (2) at RT by the flash-and-rapid-scan technique, and (3) at 20 K using the flash-and-freeze approach. For all three methods, the rate of X-ray photoreduction was studied quantitatively, leading to experimental conditions which ensure that the X-ray-induced modifications are negligible (Supporting Information, I). The obtained results do not depend critically on the details of the deconvolution procedure (Supporting Information, II−IV). Consistently, all three methods point to the same structural change in the respective S-state transition.

Prior to deconvolution, we observe an increase in the magnitude of the first two peaks in the Fourier transforms of the EXAFS oscillations in response to the second flash of light ($S_2 \rightarrow S_3$). As anticipated, this increase is enhanced, but certainly not created, by the deconvolution procedure and is fully reproducible (see the Supporting Information, III and IV). In ref *42*, however, a particularly low magnitude of the second FT peak was reported for S_3 samples. In contrast to the results in refs *42* and *43*, in this work a buffer containing 1 M glycine betaine is used and the thin, partially dehydrated samples are clearly more concentrated. Such subtle differences might affect the structure of the Mn complex in S_3. Whereas in ref *43* the X-ray dose accumulated by the PSII samples in the course of the experiment has been comparable to the maximum dose used here, in the EXAFS study reported in ref *42* the dose may have been considerably larger. Because a pronounced decrease in the magnitude of the first and second Fourier peaks results from prolonged X-ray exposure (unpublished results), this aspect of the experiments also needs to be considered as a potential source of diverging results.

The protocol used in ref *45* for the S_0-state population involved the use of FCCP, a noninnocent reagent causing destabilization of S_2 and S_3, and at higher concentrations presumably also reduction of the S_1 and S_0 complex (*5*, *87*, *88*). Nonetheless, the similarity of the EXAFS data strongly suggests that there are no relevant differences between the S_0-state created by a protocol involving ADRY reagents (in ref *45*) and the native S_0-state created purely by flash illumination (this work). In ref *45*, the presence of three Mn−Mn vectors 2.7−2.9 Å in length in the S_0 complex was suggested, a proposal mostly based on analysis of Fourier-filtered data. Avoiding this potentially misleading approach (*7*, *71*), in the work presented here, we obtained no evidence supporting the presence of three Mn−Mn distances of 2.7−2.9 Å in S_0.

Bridging-Mode Changes in the S-State Cycle. The distance between Mn ions is closely related to the connecting single-atom bridges. Comparison with synthetic models reveals the following (*89*−*96*; survey of Cambridge Structural Data Base). (i) Mn−Mn distances of 2.65−2.75 Å are exclusively found for Mn ions connected by unprotonated di-μ-oxo bridges, mostly in the form of a Mn−(μ_2-O)$_2$−Mn motif, but (rarely) also in form of a Mn−(μ_2-O)(μ_3-O)−Mn motif (discussed in ref *71*). (ii) Lengthening of the Mn−Mn distances by ∼0.1 Å is expected for protonation of one bridging oxygen in a di-μ-oxo-bridged unit, resulting in a distance of 2.8−2.9 Å in a Mn−(μ-O)(μ-OH)−Mn unit (*93*). (However, Mn−Mn distances in this range are also found for a variety of other structural motifs.) (iii) If two Mn atoms are connected by a mono-μ-oxo bridge (possibly supported by further polyatomic bridging ligands) but not by an additional μ_2-O or μ_2-OH Mn−Mn bridge, distances greater than 2.9 Å (2.9−4.0 Å) are expected. (iv) In general, changes in Mn−Mn distances of more than 0.05 Å cannot be explained by mere Mn oxidation, but by modifications of the Mn−Mn bridging mode.

In PSII, for two of the oxidizing transitions of the S-state cycle ($S_0 \rightarrow S_1$ and $S_2 \rightarrow S_3$), the Mn−Mn distances are found to change significantly, thereby immediately suggesting modifications of the Mn−Mn bridging mode. There are no indications for bridging mode changes during the $S_1 \rightarrow S_2$ transition.

For the $S_2 \rightarrow S_3$ transition, the observed increase in the number of Mn−Mn distances in the range from 2.65 to 2.8 Å can be explained by formation of a third di-μ-oxo-bridged Mn−Mn unit. The length of a single one of the three Mn−Mn vectors might be close to 2.8 Å (Table 3C) so that the presence of a singly protonated di-μ-oxo bridge is not excluded. The transformation of a mono-μ-oxo bridge (in S_1 and S_2) to a di-μ-oxo bridge (in S_3) is not proven, but compatible with the EXAFS data (disappearance of the 3.2 Å distance during the $S_2 \rightarrow S_3$ transition, Table 3B,C). The XANES spectra point toward transformation of five-coordinated Mn^{III} to six-coordinated Mn^{IV}, leading to the proposal that the terminal oxygen of a Mn^{IV} fills the vacant

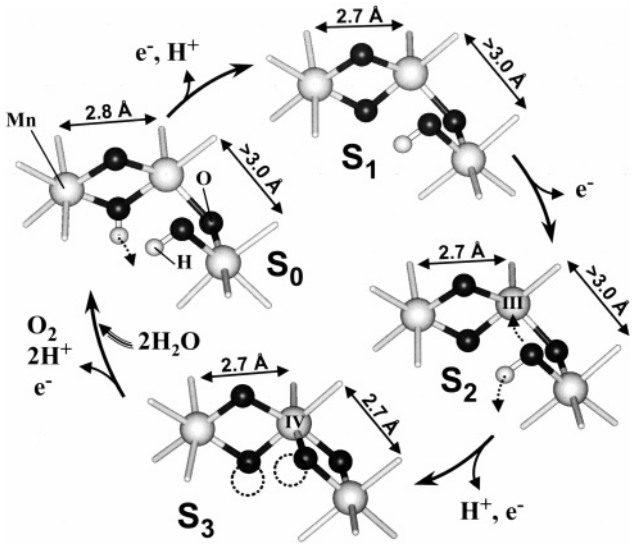

FIGURE 7: Scheme of structural changes of the Mn complex in the water oxidation cycle. For clarity, only three Mn ions of the Mn_4-Ca complex are shown which suffices to illustrate the putative modifications in the structure of the complex. The Mn−Mn distances derived from the EXAFS are indicated. The omitted fourth Mn is assumed to be connected to one of the depicted Mn ions by a di-μ-oxo bridge leading to a further Mn−Mn vector of ~2.7 Å (in all S-states). One Ca ion (not shown) presumably is connected by two or more bridging oxygens (μ-O, μ-OH, and μ-OH_2) to two or more Mn ions. As an alternative to the depicted Mn−(μ_2-O)$_2$−Mn−(μ_2-O)−Mn motif in the S_1 complex, a Mn_3−(μ_2-O)(μ_3-O) motif might be present which then is transformed into a Mn_3−(μ_2-O)$_2$(μ_3-O) unit in the $S_2 \rightarrow S_3$ transition. Single-electron oxidation of manganese is assumed to occur on $S_0 \rightarrow S_1$, $S_1 \rightarrow S_2$, and $S_2 \rightarrow S_3$ transitions, but only the oxidation state of the five-coordinated Mn^{III} (in S_2) which is transformed into a six-coordinated Mn^{IV} (in S_3) is indicated by Roman numerals inside of the respective Mn sphere. Ligand deprotonation and rearrangement presumably taking place in the subsequent S-state transition are emphasized using dotted arrows. In S_3, dotted circles mark the sites where bridging oxides may act as proton acceptors in the $S_3 \rightarrow S_0$ transition, the oxygen evolution transition.

coordination site of a previously five-coordinated Mn^{III}, thereby forming a second μ-oxo bridge between Mn ions previously connected by a single bridging oxide (Figure 7).

In S_0, the EXAFS analysis is suggestive of the presence of two Mn−Mn vectors with distinctly different lengths: one close to 2.7 Å (~2.72 Å) and the second one slightly longer than 2.8 Å (~2.84 Å). The alternative option of a single Mn−Mn vector ~2.75 Å in length is not fully excluded, but appears to be less likely. It is proposed that, during the $S_0 \rightarrow S_1$ transition, a Mn−(μ-O)(μ-OH)−Mn unit is transformed into a Mn−(μ-O)$_2$−Mn unit.

The proposed bridging-mode changes in the S-state cycle and the putative relation to (de)protonation of Mn ligands are schematically depicted in Figure 7; for a more detailed discussion, see ref *97*. We note that structural motifs as yet not covered by model chemistry might broaden the range of possibilities for translating the presented XAS data into structural models. Further studies are required to confirm the hypothetical structural cycle of Figure 7 and to obtain a more detailed picture of structural changes and localization of the accumulated oxidation equivalents.

Mechanistic Implications. In the oxidizing S-state transitions, Y_Z^{ox} successively oxidizes the Mn complex in one-electron steps. Each step is characterized by an estimated free energy change of ~100 meV (*98*), suggesting that all oxidizing S-state transitions need to proceed at a midpoint potential of the Mn complex that is by only ~100 meV lower than the Y_Z^{ox} potential [~1 V (*98*−*101*); in S_0 the potential difference might be ~250 meV (*100*)]. In a complex of four electronically coupled Mn ions, any "pure" Mn oxidation is expected to lead to a significant increase in the midpoint potential of the following oxidation step (*102*, *103*). Ligand deprotonation and especially bridging mode changes coupled to Mn oxidation may counteract the potential increase anticipated for pure Mn oxidation (*104*−*108*).

How is an approximately constant redox potential of the PSII−Mn complex maintained in four successive oxidation steps? On the basis of the EXAFS results discussed above, we propose that, on the $S_0 \rightarrow S_1$ transition, the deprotonation of a bridging hydroxide limits the potential increase. The $S_1 \rightarrow S_2$ transition, however, seems to be a pure Mn oxidation, meaning that potential-lowering deprotonation and bridging-mode changes do not take place. The potential of the thus reached S_2 complex will be too high for oxidation by Y_Z^{ox} in a pure electron transfer step. We propose that the potential-lowering deprotonation and μ-oxo bridge formation of the $S_2 \rightarrow S_3$ transition proceed prior to or, more likely, concomitantly with the $Mn_4 \rightarrow Y_Z^{ox}$ electron transfer (proton-coupled electron transfer). How the $S_3 \rightarrow S_4$ transition is facilitated remains obscure.

The presence of the di-μ-O bridges formed during the $S_0 \rightarrow S_1$ and $S_2 \rightarrow S_3$ transitions may also be mechanistically important for the $S_3 \rightarrow S_4 \rightarrow S_0$ transition, the oxygen-evolving transition itself. According to Figure 7, in the oxygen-evolving step, the bridging oxides may serve as intrinsic bases which accept protons upon the oxidation of water, thereby reversing the deprotonation events of the oxidizing S-state transitions, as discussed elsewhere in more detail (*23*). This view is in line with the observation that the water protons which are likely removed in the oxygen-evolving step mostly are not released into the bulk (*109*, *110*). In summary, a dual role of bridging oxides is proposed. (i) In the Mn-oxdizing transitions, bridging-mode changes counteract a potential increase. (ii) In the O−O bond formation step, bridging oxides facilitate water oxidation by accepting substrate-water protons.

ACKNOWLEDGMENT

We thank the staff members at the ESRF, Grenoble, and at the EMBL, Hamburg, for support and Monika Fünning (Berlin) for excellent technical assistance in the PSII preparations.

SUPPORTING INFORMATION AVAILABLE

(I) X-ray photoreduction at 20 K and RT (for all S-states), (II) determination of deconvolution parameters, (III) dependence of the EXAFS results on the deconvolution parameters, and (IV) reproducibility of the EXAFS results. This material is available free of charge via the Internet at http://pubs.acs.org.

REFERENCES

1. Debus, R. J. (1992) The manganese and calcium ions of photosynthetic oxygen evolution, *Biochim. Biophys. Acta 1102*, 269−352.

2. Nugent, J. H. A., Ed. (2001) Special Issue on Photosynthetic Water Oxidation, *Biochimica et Biophysica Acta*, Vol. 1503, Elsevier, Amsterdam.
3. Kok, B., Forbush, B., and McGloin, M. (1970) Cooperation of charges in photosynthetic O_2 evolution-I. A linear four step mechanism, *Photochem. Photobiol. 11*, 457−475.
4. Debus, R. J., Barry, B. A., Sithole, I., Babcock, G. T., and McIntosh, L. (1988) Directed mutagenesis indicates that the donor to P^{+}_{680} in photosystem II is tyrosine-161 of the D1 polypeptide, *Biochemistry 27*, 9071−9074.
5. Renger, G., and Reuter, R. (1982) The destabilization of oxidizing redox equivalents of system II by ADRY reagents in normal and Tris-washed chloroplasts, *Photobiochem. Photobiophys. 3*, 317−325.
6. Yachandra, V. K. (1995) X-ray absorption spectroscopy and applications in structural biology, in *Methods in Enzymology: Biochemical Spectroscopy* (Sauer, K., Ed.) Vol. 246, pp 638−678, Academic Press, New York.
7. Dau, H., Liebisch, P., and Haumann, M. (2003) X-ray absorption spectroscopy to analyze nuclear geometry and electronic structure of biological metal centers: potential and questions examined with special focus on the tetra-nuclear manganese complex of oxygenic photosynthesis, *Anal. Bioanal. Chem. 376*, 562−583.
8. Ascone, I., Ed. (2002) Special Issue on BioXAS, *Journal of Synchrotron Radiattion*, Vol. 10, Blackwell Publishers, Oxford, U.K.
9. Koningsberger, D. C., Mojet, B. I., Van Dorssen, G. E., and Ramaker, D. E. (2000) XAFS spectroscopy: Fundamental principles and data analysis, *Top. Catal. 10*, 143−155.
10. Scott, R. A. (2000) X-ray absorption spectroscopy, in *Physical Methods in Bioinorganic Chemistry* (Que, L., Jr., Ed.) pp 465−503, University Science Books, Sausalito, CA.
11. Bossek, U., Hummel, H., Weyhermüller, T., Wieghardt, K., Russell, S., van der Wolf, L., and Kolb, U. (1996) The $[MnIV_2(\mu\text{-}O)(\mu\text{-}PhBO_2)_2]^{2+}$ unit: A new structural model for manganese-containing metalloproteins, *Angew. Chem., Int. Ed. 35*, 1552−1554.
12. Kirby, J. A., Goodin, D. B., Wydrzynski, T., Robertson, A. S., and Klein, M. P. (1981) State of manganese in the photosynthetic apparatus. 2. X-ray absorption edge studies on manganese in photosynthetic membrane, *J. Am. Chem. Soc. 103*, 5537−5542.
13. Penner-Hahn, J. E. (1998) Structural characterization of the Mn site in the photosynthetic oxygen-evolving complex, in *Structure and Bonding: Metal Sites in Proteins and Models: Redox Centres*, pp 1−36, Springer-Verlag, Heidelberg, Germany.
14. Sauer, K., Yachandra, V. K., Britt, R. D., and Klein, M. P. (1992) The photosynthetic water oxidation complex studied by EPR and X-ray absorption spectroscopy, in *Manganese Redox Enzymes* (Pecoraro, V. L., Ed.) pp 141−175, VCH, New York.
15. Teo, B. K. (1986) *EXAFS: Basic principles and data analysis*, Springer-Verlag, Berlin.
16. Dau, H., and Haumann, M. (2003) X-ray absorption spectroscopy to watch catalysis by metalloenzymes: Status and perspectives discussed for the water-splitting manganese complex of photosynthesis, *J. Synchrotron Radiat. 10*, 76−85.
17. Penner-Hahn, J. E. (2003) Snapshots of transition states? *Nat. Struct. Biol. 10*, 75−77.
18. Cador, O., Chabre, F., Dei, A., Sangregorio, C., van Slageren, J., and Vaz, M. G. (2003) Temperature-induced solid-state valence tautomeric interconversion in two cobalt-Schiff base diquinone complexes, *Inorg. Chem. 42*, 6432−6440.
19. Rakhimov, R. R., Hawkins, T. N., Hwang, J. S., Prokof'ev, A. I., and Aleksandrov, A. I. (2003) Structure and dynamics of Bis-(triphenylphosphine)-3,6-di-*tert*-butyl-*o*-semiquinone radical anion complexes of Ag^{+} and Cu^{+}, *J. Phys. Chem. A 107*, 6345−6350.
20. Haumann, M., Müller, C., Liebisch, P., Neisius, T., and Dau, H. (2005) A novel BioXAS technique with microsecond time resolution to track oxidation state and structural changes at biological metal centers−S-state transitions of the manganese complex of oxygenic photosynthesis. *J. Synchrotron Radiat. 12*, 35−44.
21. Haumann, M., Grabolle, M., Neisius, T., and Dau, H. (2002) The first room-temperature X-ray absorption spectra of higher oxidation states of the tetra-manganese complex of photosystem II, *FEBS Lett. 512*, 116−120.
22. Meinke, C., Sole, V. A., Pospisil, P., and Dau, H. (2000) Does the structure of the water-oxidizing photosystem II-manganese complex at room temperature differ from its low-temperature structure? A comparative X-ray absorption study, *Biochemistry 39*, 7033−7040.
23. Dau, H., Iuzzolino, L., and Dittmer, J. (2001) The tetra-manganese complex of photosystem II during its redox cycle: X-ray absorption results and mechanistic implications, *Biochim. Biophys. Acta 1503*, 24−39.
24. MacLachlan, D. J., Nugent, J. H., Bratt, P. J., and Evans, M. C. W. (1994) The effects of calcium depletion in the O_2-evolving complex in spinach PS II: The S_1, S_2 and S_3 states and the role of the 17 kDa and 23 kDa extrinsic polypeptides, *Biochim. Biophys. Acta 1186*, 186−200.
25. Ono, T., Noguchi, T., Inoue, Y., Kusunoki, M., Matsushita, T., and Oyanagi, H. (1992) X-ray detection of the period-four cycling of the manganese cluster in photosynthetic water oxidizing enzyme, *Science 258*, 1335−1337.
26. Robblee, J. H., Cinco, R. M., and Yachandra, V. K. (2001) X-ray spectroscopy-based structure of the Mn cluster and mechanism of photosynthetic oxygen evolution, *Biochim. Biophys. Acta 1503*, 7−23.
27. Yachandra, V. K., DeRose, V. J., Latimer, M. J., Mukerji, I., Sauer, K., and Klein, M. P. (1993) Where plants make oxygen: A structural model for the photosynthetic oxygen-evolving manganese cluster, *Science 260*, 675−679.
28. Yachandra, V. K. (2002) Structure of the manganese complex in photosystem II: Insights from X- ray spectroscopy, *Philos. Trans. R. Soc. London, Ser. B 357*, 1347−1357.
29. De Paula, J. C., Innes, J. B., and Brudvig, G. W. (1985) Electron transfer in photosystem II at cryogenic temperatures, *Biochemistry 24*, 8114−8120.
30. Zhang, C., and Styring, S. (2003) Formation of split electron paramagnetic resonance signals in photosystem II suggests that tyrosine Z can be photooxidized at 5 K in the S_0 and S_1 states of the oxygen-evolving complex, *Biochemistry 42*, 8066−8076.
31. Ioannidis, N., and Petrouleas, V. (2000) Electron paramagnetic resonance signals from the S_3 state of the oxygen-evolving complex. A broadened radical signal induced by low-temperature near-infrared light illumination, *Biochemistry 39*, 5246−5254.
32. Ioannidis, N., and Petrouleas, V. (2002) Decay products of the S_3 state of the oxygen-evolving complex of photosystem II at cryogenic temperatures. Pathways to the formation of the $S = 7/2$ S_2 state configuration, *Biochemistry 41*, 9580−9588.
33. Ioannidis, N., Nugent, J. H., and Petrouleas, V. (2002) Intermediates of the S_3 state of the oxygen-evolving complex of photosystem II, *Biochemistry 41*, 9589−9600.
34. Nugent, J. H., Turconi, S., and Evans, M. C. (1997) EPR investigation of water oxidizing photosystem II: Detection of new EPR signals at cryogenic temperatures, *Biochemistry 36*, 7086−7096.
35. Nugent, J. H., Muhiuddin, I. P., and Evans, M. C. (2002) Electron transfer from the water oxidizing complex at cryogenic temperatures: The S_1 to S_2 step, *Biochemistry 41*, 4117−4126.
36. Burda, K., Bader, K. P., and Schmid, G. H. (2003) ^{18}O isotope effect in the photosynthetic water splitting process, *Biochim. Biophys. Acta 1557*, 77−82.
37. Renger, G., and Hanssum, B. (1992) Studies on the reaction coordinates of the water oxidase in PS II membrane fragments from spinach, *FEBS Lett. 299*, 28−32.
38. Burda, K., and Schmid, G. H. (2001) Heterogeneity of the mechanism of water splitting in photosystem II, *Biochim. Biophys. Acta 1506*, 47−54.
39. Messinger, J. (2000) Towards understanding the chemistry of photosynthetic oxygen evolution: Dynamic structural changes, redox states and substrate water binding of the Mn cluster in photosystem II, *Biochim. Biophys. Acta 1459*, 481−488.
40. Renger, G., Christen, G., Karge, M., Eckert, H. J., and Irrgang, K.-D. (1998) Application of the Marcus theory for analysis of the temperature dependence of the reactions leading to photosynthetic water oxidation: Results and implications, *J. Biol. Inorg. Chem. 3*, 360−366.
41. Iuzzolino, L., Dittmer, J., Dorner, W., Meyer-Klaucke, W., and Dau, H. (1998) X-ray absorption spectroscopy on layered photosystem II membrane particles suggests manganese-centered oxidation of the oxygen-evolving complex for the S_0-S_1, S_1-S_2, and S_2-S_3 transitions of the water oxidation cycle, *Biochemistry 37*, 17112−17119.
42. Liang, W., Roelofs, T. A., Cinco, R. M., Rompel, A., Latimer, M. J., Yu, W. O., Sauer, K., Klein, M. P., and Yachandra, V. K. (2000) Structural change of the Mn cluster during the S_2-S_3 state transition of the oxygen-evolving complex of photosystem II. Does

it reflect the onset of water/substrate oxidation? Determination by Mn X-ray absorption spectroscopy, *J. Am. Chem. Soc. 122*, 3399−3412.
43. Messinger, J., Robblee, J. H., Bergmann, U., Fernandez, C., Glatzel, P., Visser, H., Cinco, R. M., McFarlane, K. L., Bellacchio, E., Pizarro, S. A., Cramer, S. P., Sauer, K., Klein, M. P., and Yachandra, V. K. (2001) Absence of Mn-centered oxidation in the $S_2 \rightarrow S_3$ transition: Implications for the mechanism of photosynthetic water oxidation, *J. Am. Chem. Soc. 123*, 7804−7820.
44. Roelofs, T. A., Liang, W., Latimer, M. J., Cinco, R. M., Rompel, A., Andrews, J. C., Sauer, K., Yachandra, V. K., and Klein, M. P. (1996) Oxidation states of the manganese cluster during the flash-induced S-state cycle of the photosynthetic oxygen-evolving complex, *Proc. Natl. Acad. Sci. U.S.A. 93*, 3335−3340.
45. Robblee, J. H., Messinger, J., Cinco, R. M., McFarlane, K. L., Fernandez, C., Pizarro, S. A., Sauer, K., and Yachandra, V. K. (2002) The Mn cluster in the S_0 state of the oxygen-evolving complex of photosystem II studied by EXAFS spectroscopy: Are there three di-μ-oxo-bridged Mn_2 moieties in the tetranuclear Mn complex? *J. Am. Chem. Soc. 124*, 7459−7471.
46. Berthold, D. A., Babcock, G. T., and Yocum, C. F. (1981) A highly resolved, oxygen-evolving photosystem II preparation from spinach thylakoid membranes, *FEBS Lett. 134*, 231−234.
47. Schiller, H., and Dau, H. (2000) Preparation protocols for high-activity photosystem II membrane particles of green algae and higher plants, pH dependence of oxygen evolution and comparison of the S_2-state multiline signal by X-band EPR spectroscopy, *J. Photochem. Photobiol., B 55*, 138−144.
48. Dismukes, G. C., and Siderer, Y. (1981) Intermediates of a polynuclear manganese center involved in photosynthetic oxidation of water, *Proc. Natl. Acad. Sci. U.S.A. 78*, 274−278.
49. Miller, A. F., and Brudvig, G. W. (1991) A guide to electron paramagnetic resonance spectroscopy of photosystem II membranes, *Biochim. Biophys. Acta 1056*, 1−18.
50. Boussac, A., Girerd, J. J., and Rutherford, A. W. (1996) Conversion of the spin state of the manganese complex in photosystem II induced by near-infrared light, *Biochemistry 35*, 6984−6989.
51. Boussac, A., and Rutherford, A. W. (2000) Comparative study of the $g = 4.1$ EPR signals in the S_2 state of photosystem II, *Biochim. Biophys. Acta 1457*, 145−156.
52. Sole, V. A., Gauthier, C., Goulon, J., and Natali, F. (1999) Undulator QEXAFS at the ESRF beamline ID26, *J. Synchrotron Radiat. 6*, 174−175.
53. Dittmer, J., and Dau, H. (1998) Theory of the linear dichroism in the extended X-ray absorption fine structure (EXAFS) of partially vectorially ordered systems, *J. Phys. Chem. B 102*, 8196−8200.
54. Schiller, H., Dittmer, J., Iuzzolino, L., Dorner, W., Meyer-Klaucke, W., Sole, V. A., Nolting, H., and Dau, H. (1998) Structure and orientation of the oxygen-evolving manganese complex of green algae and higher plants investigated by X-ray absorption linear dichroism spectroscopy on oriented photosystem II membrane particles, *Biochemistry 37*, 7340−7350.
55. Dittmer, J. (1999) Linear Dichroismus-Röntgenabsorptionsspektroskopie zum katalytischen Zyklus des wasserspaltenden Mangankomplexes der Photosynthese in Theorie und Experiment, Ph.D. Thesis, Christian Albrechts Universität, Kiel, Germany.
56. Rehr, J. J., Mustre de Leon, J., Zabinsky, S. I., and Albers, R. C. (1991) Theoretical X-ray absorption fine structure standards, *J. Am. Chem. Soc. 113*, 5135−5140.
57. Pospisil, P., Haumann, M., Dittmer, J., Sole, V. A., and Dau, H. (2003) Stepwise transition of the tetra-manganese complex of photosystem II to a binuclear $Mn_2(\mu\text{-}O)_2$ complex in response to a temperature jump: A time-resolved structural investigation employing X-ray absorption spectroscopy, *Biophys. J. 84*, 1370−1386.
58. Dau, H., Dittmer, J., Iuzzolino, L., Schiller, H., Dörner, W., Heinze, I., Sole, V. A., and Nolting, H.-F. (1997) X-ray absorption linear dichroism spectroscopy (XALDS) on the photosystem II manganese complex: Radiation damage and S_1-state K-edge spectra, *J. Phys. IV 7*, 607−610.
59. Dittmer, J., Iuzzolino, L., Dorner, W., Nolting, H.-F., Meyer-Klaucke, W., and Dau, H. (1998) A new method for determination of the edge position of X-ray absorption spectra, in *Photosynthesis: Mechanisms and Effects* (Garab, G., Ed.) pp 1339−1342, Kluwer Academic Publishers, Budapest.
60. Ferreira, K. N., Iverson, T. M., Maghlaoui, K., Barber, J., and Iwata, S. (2004) Architecture of the photosynthetic oxygen-evolving center, *Science 303*, 1831−1838.
61. Kamiya, N., and Shen, J. R. (2003) Crystal structure of oxygen-evolving photosystem II from *Thermosynechococcus vulcanus* at 3.7-Å resolution, *Proc. Natl. Acad. Sci. U.S.A. 100*, 98−103.
62. Debus, R. J., Campbell, K. A., Peloquin, J. M., Pham, D. P., and Britt, R. D. (2000) Histidine 332 of the D1 polypeptide modulates the magnetic and redox properties of the manganese cluster and tyrosine Y_Z in photosystem II, *Biochemistry 39*, 470−478.
63. Debus, R. J., Campbell, K. A., Pham, D. P., Hays, A. M., and Britt, R. D. (2000) Glutamate 189 of the D1 polypeptide modulates the magnetic and redox properties of the manganese cluster and tyrosine Y_Z in photosystem II, *Biochemistry 39*, 6275−6287.
64. Debus, R. J. (2001) Amino acid residues that modulate the properties of tyrosine Y_Z and the manganese cluster in the water oxidizing complex of photosystem II, *Biochim. Biophys. Acta 1503*, 164−186.
65. Diner, B. A. (2001) Amino acid residues involved in the coordination and assembly of the manganese cluster of photosystem II. Proton-coupled electron transport of the redox-active tyrosines and its relationship to water oxidation, *Biochim. Biophys. Acta 1503*, 147−163.
66. Cinco, R. M., McFarlane Holman, K. L., Robblee, J. H., Yano, J., Pizarro, S. A., Bellacchio, E., Sauer, K., and Yachandra, V. K. (2002) Calcium EXAFS establishes the Mn−Ca cluster in the oxygen-evolving complex of photosystem II, *Biochemistry 41*, 12928−12933.
67. Latimer, M. J., DeRose, V. J., Mukerji, I., Yachandra, V. K., Sauer, K., and Klein, M. P. (1995) Evidence for the proximity of calcium to the manganese cluster of photosystem II: Determination by X-ray absorption spectroscopy, *Biochemistry 34*, 10898−10909.
68. Latimer, M. J., DeRose, V. J., Yachandra, V. K., Sauer, K., and Klein, M. P. (1998) Structural effects of calcium depletion in the manganese cluster in photosystem II: Determination by X-ray absortption spectroscopy, *J. Phys. Chem. B 102*, 8257−8265.
69. Müller, C., Liebisch, P., Barra, M., Dau, H., and Haumann, M. (2002) The location of calcium in the manganese complex of oxygenic photosynthesis studied by X-ray absorption spectroscopy at the Ca K-edge, *Phys. Scr.* (in press).
70. Dörner, W., Dittmer, J., Iuzzolino, L., Meyer-Klaucke, W., and Dau, H. (1998) The structure of a partially assembled, di-nuclear PS II manganese complex investigated by EPR and EXAFS on a new core complex preparation, in *Photosynthesis: Mechanisms and Effects* (Garab, G., Ed.) pp 1343−1346, Kluwer Academic Publishers, Budapest.
71. Dau, H., Liebisch, P., and Haumann, M. (2004) The structure of the manganese complex of photosystem II in its dark-stable S_1-state: EXAFS results in relation to recent crystallographic data, *Phys. Chem. Chem. Phys. 6*, 4781−4792.
72. Gilbert, B., Frazer, B. H., Belz, A., Conrad, P. G., Nealson, K. H., Haskel, D., Lang, J. C., Srajer, G., and De Stasio, G. (2003) Multiple scattering calculations of bonding and X-ray absorption spectroscopy of manganese oxides, *J. Phys. Chem. A 107*, 2839−2847.
73. Visser, H., Anxolabehere-Mallart, E., Bergmann, U., Glatzel, P., Robblee, J. H., Cramer, S. P., Girerd, J. J., Sauer, K., Klein, M. P., and Yachandra, V. K. (2001) Mn K-edge XANES and K_β XES studies of two Mn-oxo binuclear complexes: Investigation of three different oxidation states relevant to the oxygen-evolving complex of photosystem II, *J. Am. Chem. Soc. 123*, 7031−7039.
74. Waldo, G. S., Fronko, R. M., and Penner-Hahn, J. E. (1991) Inactivation and reactivation of manganese catalase: Oxidation-state assignments using X-ray absorption spectroscopy, *Biochemistry 30*, 10486−10490.
75. Ankudinov, A. L., Ravel, B., and Conradson, S. D. (1998) Real-space multiple-scattering calculation and interpretation of X-ray-absorption near-edge structure, *Phys. Rev. B 58*, 7565−7576.
76. Dau, H., Liebisch, P., and Haumann, M. (2004) The manganese complex of oxygenic photosynthesis: Conversion of five-coordinated Mn(III) to six-coordinated Mn(IV) in the S_2-S_3 transition is implied by XANES simulations, *Phys. Scr.* (in press).
77. Colpas, G. J., Maroney, M. J., Bagyinka, C., Kumar, M., Willis, W. S., Suib, S. L., Mascharak, P. K., and Baidya, N. (1991) X-ray spectroscopic studies of nickel complexes, with application to the structure of nickel sites in hydrogenases, *Inorg. Chem. 30*, 920−928.
78. Feiters, M. C., Eijkelenboom, A. P., Nolting, H. F., Krebs, B., van den Ent, F. M., Plasterk, R. H., Kaptein, R., and Boelens, R. (2003) X-ray absorption spectroscopic studies of zinc in the N-terminal domain of HIV-2 integrase and model compounds, *J. Synchrotron Radiat. 10*, 86−95.

79. Haumann, M., Porthun, A., Buhrke, T., Liebisch, P., Meyer-Klaucke, W., Friedrich, B., and Dau, H. (2003) Hydrogen-induced structural changes at the nickel site of the regulatory [NiFe] hydrogenase from *Ralstonia eutropha* detected by X-ray absorption spectroscopy, *Biochemistry 42*, 11004−11015.
80. Scarrow, R. C., Trimitsis, M. G., Buck, C. P., Grove, G. N., Cowling, R. A., and Nelson, M. J. (1994) X-ray spectroscopy of the iron site in soybean lipoxygenase-1: Changes in coordination upon oxidation or addition of methanol, *Biochemistry 33*, 15023−15035.
81. Bergmann, U., Grush, M. M., Horne, C. R., Demarois, P., Penner-Hahn, J. E., Yocum, C. F., Wright, D. W., Dube, C. E., Armstrong, W. H., Christou, G., Eppley, H. J., and Cramer, S. P. (1998) Characterization of the Mn Oxidation States in Photosystem II by K_β X-ray Fluorescence Spectroscopy, *J. Phys. Chem. B 102*, 8350−8352.
82. Peng, G., de Groot, F. M. F., Hamalainen, K., Moore, J. A., Wang, X., Grush, M. M., Hastings, J. B., Siddons, D. P., Armstrong, W. H., Mullins, O. C., and Cramer, S. P. (1994) High-resolution manganese X-ray fluorescence spectroscopy. Oxidation-state and spin-state sensitivity, *J. Am. Chem. Soc. 116*, 2914−2920.
83. Cole, J., Yachandra, V. K., Guiles, R. D., McDermott, A. E., Britt, R. D., Dexheimer, S. L., Sauer, K., and Klein, M. P. (1987) Assignment of the $g = 4.1$ EPR signal to manganese in the S_2 state of the photosynthetic oxygen-evolving complex: An X-ray absorption edge spectroscopy study, *Biochim. Biophys. Acta 890*, 395−398.
84. Guiles, R. D., Yachandra, V. K., McDermott, A. E., Cole, J. L., Dexheimer, S. L., Britt, R. D., Sauer, K., and Klein, M. P. (1990) The S0 state of photosystem II induced by hydroxylamine: Differences between the structure of the manganese complex in the S0 and S1 states determined by X-ray absorption spectroscopy, *Biochemistry 29*, 486−496.
85. Carrell, G., Tyryshkin, M., and Dismukes, C. (2002) An evaluation of structural models for the photosynthetic water-oxidizing complex derived from spectroscopic and X-ray diffraction signatures, *J. Biol. Inorg. Chem. 7*, 2−22.
86. Kuzek, D., and Pace, R. J. (2001) Probing the Mn oxidation states in the OEC. Insights from spectroscopic, computational and kinetic data, *Biochim. Biophys. Acta 1503*, 123−137.
87. Ghanotakis, D. F., Yerkes, C. T., and Babcock, G. T. (1982) The role of reagents accelerating the deactivation reactions of water-splitting enzyme system Y (ADRY reagents) in destabilizing high-potential oxidizing equivalents generated in chloroplast photosystem II, *Biochim. Biophys. Acta 682*, 21−31.
88. Renger, G. (1972) The action of 2-anilinothiophenes as accelerators of the deactivation reactions in the water-splitting enzyme system of photosynthesis, *Biochim. Biophys. Acta 256*, 428−439.
89. Armstrong, W. H. (1992) Polynuclear manganese complexes as models for the photosystem II water oxidation catalyst, in *Manganese Redox Enzymes* (Pecoraro, V. L., Ed.) pp 261−286, VCH, New York.
90. Pecoraro, V. L., (1992) Structurally diverse manganese coordination complexes: From voodoo to oxygenic photosynthesis, *Manganese Redox Enzymes*, (Pecoraro, V. L., Ed.) pp 197−231, VCH, New York.
91. Pecoraro, V. L., and Hsieh, W.-Y. (2000) The use of model complexes to elucidate the structure and function of manganese redox enzymes, *Met. Ions Biol. Syst. 37*, 429−504.
92. Wieghardt, K. (1989) Die aktiven Zentren in manganhaltigen Metallproteinen und anorganische Modellkomplexe, *Angew. Chem. 101*, 1179−1198.
93. Baldwin, M. J., Law, N. A., Stemmler, T. L., Kampf, J. W., Penner-Hahn, J. E., and Pecoraro, V. L. (1999) Reactivity of $[\{MnIV(salpn)\}_2(\mu\text{-}O,\mu\text{-}OCH_3)]^+$ and $[\{MnIV(salpn)\}_2(\mu\text{-}O,\mu\text{-}OH)]^+$: Effects of proton lability and hydrogen bonding, *Inorg. Chem. 38*, 4801−4809.
94. Christou, G. (1989) Manganese carboxylate chemistry and its biological relevance, *Acc. Chem. Res. 22*, 328−335.
95. Larson, E. J., and Pecoraro, V. L. (1992) Introduction to Manganese Enzymes, in *Manganese Redox Enzymes* (Pecoraro, V. L., Ed.) VCH, New York.
96. Hagen, K. S., Armstrong, W. H., and Olmstead, M. M. (1989) $[Mn_{10}O_4[N(CH_2CH_2NH_2)_3]_6]^{8+}$: A mixed-valence polyoxomanganese polycation possessing structural similarities to naturally occurring layered manganese oxides, *J. Am. Chem. Soc. 111*, 774−775.
97. Dau, H., Liebisch, P., and Haumann, M. (2004) Structural and oxidation state changes of the Mn_4Ca complex of photosystem II in its S-state cycle: X-ray absorption results and possible mechanistic implications, *Proceedings of 13th International Congress on Photosynthesis* (in press).
98. Vos, M. H., van Gorkom, H. J., and van Leeuwen, P. J. (1991) An electroluminescence study of stabilization reactions in the oxygen-evolving complex of photosystem II, *Biochim. Biophys. Acta 1056*, 27−39.
99. Geijer, P., Morvaridi, F., and Styring, S. (2001) The S_3 state of the oxygen-evolving complex in photosystem II is converted to the S_2Y_Z* state at alkaline pH, *Biochemistry 40*, 10881−10891.
100. Vass, I., and Styring, S. (1991) pH-dependent charge equilibria between tyrosine-D and the S states in photosystem II. Estimation of relative midpoint redox potentials, *Biochemistry 30*, 830−839.
101. Yerkes, C. T., Babcock, G. T., and Crofts, A. R. (1983) A Tris-induced change in the midpoint potential of Z, the donor to photosystem II, as determined by the kinetics of the back reaction, *FEBS Lett. 158*, 359−363.
102. Goodson, P. A., Glerup, J., and Hodgson, D. J. (1990) Binuclear bis(μ-oxo)dimanganese(III,IV) and -(IV,IV) complexes with N,N′-bis(2-pyridylmethyl)-1,2-ethanediamine, *Inorg. Chem. 29*, 503−508.
103. Mandal, S. K., and Armstrong, W. H. (1995) A novel triply bridged dinuclear manganese(III) complex containing the $[Mn_2O(OAc)_2]^{2+}$ core: Synthesis, crystal structure and properties of $[Mn_2(\mu\text{-}O)(\mu\text{-}OAc)_2(bpea)_2](ClO_4)_2$, *Inorg. Chim. Acta 229*, 261−270.
104. Baldwin, M. J., and Pecoraro, V. L. (1996) Energetics of proton-coupled electron transfer in high-valent $Mn_2(\mu\text{-}O)_2$ systems: Models for water oxidation by the oxygen-evolving complex of photosystem II, *J. Am. Chem. Soc. 118*, 11325−11326.
105. Boelrijk, A. E. M., Khangulov, S. V., and Dismukes, G. C. (2000) Bridging Hydroxide Effect on Carboxylato Coordination and Electrochemical Potentials of Bimetallic Centers: Mn_2(II,II) and Mn_2(III,III) Complexes as Functional Models of Dimanganese Catalases, *Inorg. Chem. 39*, 3009−3019.
106. Lal, T. K., and Mukherjee, R. (1998) Modeling the oxygen-evolving complex of photosystem II. Synthesis, redox properties, and core interconversion studies of dimanganese complexes having $\{MnIII_2(\mu\text{-}O)(\mu\text{-}OAc)_2\}^{2+}$, $\{MnIIIMnIV(\mu\text{-}O)^2(\mu\text{-}OAc)\}^{2+}$, and $\{MnIV_2(\mu\text{-}O)_2(\mu\text{-}OAc)\}^{3+}$ cores with MeL as a terminal ligand: A new asymmetric mixed-valence core, *Inorg. Chem. 37*, 2373−2382.
107. Tanase, T., and Lippard, S. J. (1995) Dinuclear manganese(II) complexes with the $\{Mn_2(\mu\text{-carboxylato})_2\}^{2+}$ core and their transformation to (μ-oxo)bis(μ-carboxylato)dimanganese(III) complexes, *Inorg. Chem. 34*, 4682−4690.
108. Manchanda, R., Holden, T. H., Brudvig, G. W., and Crabtree, R. H. (1991) Proton-coupled electron transfer in high-valent oxomanganese dimers: Role of the ancillary ligands, *Inorg. Chem. 30*, 494−497.
109. Förster, V., and Junge, W. (1985) Stoichiometry and kinetics of proton release upon photosynthetic water oxidation, *Photochem. Photobiol. 41*, 183−190.
110. Haumann, M., and Junge, W. (1994) Extent and rate of proton release by photosynthetic water oxidation in thylakoids: Electrostatic relaxation versus chemical production, *Biochemistry 33*, 864−872.

BI048697E